이학박사학위논문

Thin-film Superconductor FeSe
: Scanning Tunneling Microscopy Study

박막 아이언 셀레나이드 초전도체
: 주사형 탐침 현미경 연구

2017년 8월

서울대학교 대학원

물리천문학부

이민준

Thin-film Superconductor FeSe

: Scanning Tunneling Microscopy Study

박막 아이언 셀레나이드 초전도체

: 주사형 탐침 현미경 연구

지도교수 국 양

이 논문을 이학박사 학위논문으로 제출함

2017년 5월

서울대학교 대학원

물리천문학부

이민준

이민준의 이학박사 학위논문을 인준함

2017년 6월

위 원 장 최 석 봉 (인)

부위원장 국 양 (인)

위 원 차 국 린 (인)

위 원 박 철 환 (인)

위 원 서 정 필 (인)

Abstract

Thin-film Superconductor FeSe

: Scanning Tunneling Microscopy Study

Minjun Lee

Department of Physics and Astronomy

The Graduate School

Seoul National University

Since the discovery of superconducting phenomena by H. K. Onnes in 1911[1], superconductors have become a major research field in the solid states physics. Numerous physicists have discovered new superconductors and are working to physically explain superconductivity phenomena. In surface science, superconductors are also an interesting research topic. It mainly studies how low-dimensional physical phenomena appear in superconductors and how superconductivity itself changes at low dimension. I have studied superconductivity phenomenon in low dimension, especially two dimension, using scanning tunneling microscope (STM). The superconducting samples used in the study are tetragonal FeSe on $SrTiO_3$(100) and hexagonal FeSe on $SrTiO_3$(100). Tetragonal FeSe has the

simplest structure among the iron chalcogenide superconductor. In 2012, the Xue's group in China found that when 1 ML FeSe was grown on $SrTiO_3$(100), the critical temperature rose to over 60 K [2], many physicists have gone into this study and tried to figure out why the critical temperature has improved . This study was initiated to clarify the pairing mechanism of tetragonal FeSe on $SrTiO_3$(100). I analyzed the spectroscopy of STM and found the frequency of the bosonic mode that is involved in the Cooper pairing using the Eliashberg model. And I tried to find out what the expected bosonic mode is. Next, hexagonal FeSe, which is a new phase of FeSe, was grown on $SrTiO_3$(100) and its physical properties were measured using STM. The newly discovered hexagonal phase FeSe shows many experimental results consistent with the superconducting phenomenon, but further studies are needed to confirm it as a new superconductor.

Keywords : superconductor, thin-film superconductor, iron selenide, scanning tunneling microscopy

Student Number : 2009-20420

Contents

List of Figures

Chapter 1. Introduction to Superconductivity

Physicists are constantly studying superconductivity and new superconductors are also being discovered [1], [3], [4]. The studies of superconductivity have attempted to discover new materials that maintain superconductivity even at higher temperatures [3], [4], as well as to explore what is the root cause of superconductivity and to further predict their properties[5]. There is a driving force to enrich human life and conserve the natural resources on the basis of efforts to raise superconducting critical temperature from low temperature to high temperature, even to room temperature. There are many examples where superconductivity is actually applied [6], [7]. Superconducting coils can generate and maintain a high magnetic field because they can maintain a large amount of current without loss. These superconducting coils are used in magnetic resonance imaging (MRI) in hospitals and as particle accelerators in particle physics. In other words, it not only makes human life healthy, but it also helps to develop other physics fields. The superconducting quantum interference device (SQUID) using Josephson phenomena during superconducting phenomena is a device that can detect very small magnetic field, about 10^{-15} T. It is applied to the medical field because it can measure the magnetic field generated by the human brain (10^{-12} to 10^{-13} T) or the vertebrae (10^{-14} T) [8]. In addition, the superconducting quantum cubit is one of the candidates to be used as a cubit, a building block in the quantum computer field.

As the temperature at which superconductivity is maintained increases, some revolution occur in many ways. First, the MRI described above uses liquid helium as a refrigerant, which causes a large maintenance cost and

therefore a large burden on the patient. However, if a superconducting coil is found above liquid nitrogen or dry ice temperatures, a major revolution in the medical profession will emerge. Compared to liquid helium, liquid nitrogen is about one tenth cheap and dry ice is not to mention. If a room temperature superconductor is manufactured, it can be used as a magnetically levitated train or a wire without power loss, so that resources can be used without waste.

The desire for such a high-temperature superconductor is being realized in the history of superconductivity. In 1911, K. H. Onnes [1] discovered a superconducting phenomenon at a cryogenic temperature of 4.3 K in mercury and then found a high-temperature superconducting phenomenon of over 90 K in the copper perovskite ceramic material that was discovered in 1986 [3]. In addition, since iron-based superconductors were discovered in 2008 [4], superconductivity of T_c = 100K was observed when FeSe was stacked on the STO [2]. This dream of high-temperature superconductors is being realized, and many scientists are studying it enthusiastically because it appears beautiful and interesting in various forms beyond simplicity.

So, how have these superconducting materials been discovered? Since the first superconducting phenomenon was discovered in mercury in 1911 [1], many superconducting phenomena have been found in metallic single elements, and superconducting phenomena have been stereotyped to appear to be unlikely to occur in nonconductive ceramics. However, in 1986, the discovery of high-temperature superconducting phenomena in copper-oxide-ceramic-based materials has shattered this existing myth [3]. In addition, no superconducting phenomenon occurred in magnetic elements

such as Fe, Co, and Mn, and when the magnetic field was applied, superconductivity disappeared, and no one could predict that superconductivity would occur in iron-based materials. In 2008, however, the myth of the scientific community broke up nicely, and iron-based high-temperature superconductors, like copper-oxide superconductors, have been discovered to form another superconductor family [4]. This history of superconducting material discovery seems to be a history that breaks the myth of scientists, a history of the collapse of the human reason.

However, the history of explaining superconducting phenomena and discovering its underlying mechanism still demonstrates the incredible sophistication and beauty of scientific thinking. The superconductor family, first discovered and developed in 1911 from mercury [1], is called a conventional superconductor to distinguish it from a high-temperature superconductor. The superconductivity in a conventional superconductor can be explained well by the pairing of two electrons via the attractive interaction between them. This pairing is called the Cooper pair, and this theory is called the BCS theory (1957) [5]. The BCS theory is a beautiful and sophisticated theory that was completed by the work of Prof. J. Bardeen, Dr. L. N. Cooper, and student J. R. Schrieffer. Many scientists challenged the phenomenon of superconductivity, which was the subject of solid-state physics at that time but failed to reveal its fundamental mechanism. However, Cooper's idea, Schrieffer's perseverance and the expertise of Bardeen who guided it led to the theory of microscopic explanation of superconductivity. BCS theory is a masterpiece of a beautiful masterpiece in the scientific community.

So what is the fundamental reality of the superconductivity phenomenon

in this theory? Cooper envisioned a superconducting phenomenon in which two electrons attractively interact in the medium for some reason. And the reality that enables the attractive interaction is phonon mode. This idea became the seed and the ground state was correctly described, and the superconductivity was finally solved. Since then, unconventional superconductors, which are not solved by the BCS theory, have begun to be found, which is a challenging problem and waiting for someone's hand.

In this study, Fe chalcogenide in Fe - based superconductor were studied using Scanning Tunneling Microscope. Following the study of tetragonal FeSe in the midst of Fe chalcogenide, a new hexagonal phase of FeSe was studied. In the tetragonal phase, Scanning tunneling microscopy and inelastic electron tunneling spectroscopy (STM-IETS) method was applied to study bosonic mode. In hexagonal phase, STM was used to perform initial image, spectroscopy, and IETS. I hope this research becomes another small seed in the superconductor study.

1.1 Conventional Superconductor

Since the idea of Cooper, superconductivity is explained by the phenomenon of attractive interaction between two bosonic modes. One of the bosonic modes is phonon. In this session, we will briefly study about basic theory of superconductor so-called BCS theory. Next, we will focus the phonon mediated superconductivity.

1.1.1 Basic Introduction

Resistance is a physical phenomenon that occurs because of the collision of electron and phonon and the collision of electron and electron. When the temperature is lowered, the phonons freeze out, reducing collisions between electrons and phonons, and also reducing collisions between electrons and electrons [9]. However, since there is the imperfection of the inevitable lattice or collision with impurities, it has been expected that the resistance will never become 0 even at an absolute temperature of 0 K. However, in 1911, H. Kamerlingh Onnes observed that mercury abruptly dropped resistance at liquid helium temperature and became a perfect conductor [1]. This was an important discovery that broke conventional expectations and was the beginning of superconductors.

In 1933, another property of superconductors was discovered by W. Meissner and R. Ochsenfeld [10]. That is, it has perfect diamagnetism. That is, the magnetic susceptibility of a superconductor is $\chi = -1$. The physical reality of this phenomenon is the fact that the magnetic field cannot penetrate into the superconductor by expelling the externally applied magnetic field. This can be achieved by applying a magnetic field first and then lowering it to a superconducting temperature, which is also achieved by applying a magnetic field at a superconducting temperature. That is, regardless of the past history of the sample.

In 1935, F. and H. London developed a phenomenological equation of superconductivity based on Maxwell's equation and Drude equation [11]. London explains that the charge carrier of a superconductor is divided into a normal charge carrier and a superconducting charge carrier. It is assumed

that the density of superconducting charge carrier increases from 0 as the temperature falls below Tc. This theory quantitatively explained the Meissner effect and showed that the magnetic field can penetrate the superconductor with a London penetration depth.

There is another macroscopic and phenomenological theory, called Ginsburg-Landau theory. In 1950, V. L. Ginsburg and L.D. Landau tried to explain the superconducting state as a framework of Landau's general theory of phase transition [12]. The order parameter causing the phase transition is set as the superconducting charge density. This theory is easy to deal with the spatial variation of the superconducting charge density. For example, A. Abrikosov divided the superconductor into two types using the Ginsburg-Landau theory [13]. Type II with a Vortex lattice and type I not. The London equation and the Ginsburg-Landau theory illustrate the specific properties of superconductivity but do not present a fundamental cause, namely, a microscopic picture.

The microscopic theory of the first attempted and successfully completed about superconductivity is the BCS theory [5]. In 1957, J. Bardeen, L. N. Cooper, and J. R. Schrieffer described the first microscopic picture of superconductivity. The core of the BCS theory is the idea that the fermi sea, a ground state in a normal metal, will become unstable when there is an attractive interaction between electron and electron, resulting in another ground state. Here, Bardeen, Cooper, and Schrieffer have considered the phonon as a candidate for possible attractive interaction. This is because of the isotope effect [14]. It says superconducting critical temperature Tc, was observed to be proportional to $1 / \sqrt{M}$. This experimental result indicates that

the critical temperature is related to the frequency of the lattice vibration. Bardeen, Cooper, and Schrieffer predict that the phonon will affect the interaction based on this fact. Based on this prediction, they constructed and applied phonon mediated electron pairing, i.e. Cooper pair, to complete the BCS theory. Furthermore, any exchange bosonic mode other than phonons, such as magnons, polarons, or plasmons, can also affect the attractive interaction.

1.1.2 BCS Theory

In the BCS Theory, the energy of the two electrons with an attractive interaction is as follows [7], [15].

$$E_{pair} = 2E_F - \frac{2\hbar\omega_c e^{-2/D(E_F)V_0}}{1 - e^{-2/D(E_F)V_0}} \quad (1)$$

Here $\hbar\omega_c$ is the characteristic energy of the exchange bosons. V_0 is the strength of the interaction potential and $D(E_F)$ the electron density of state in normal state at the Fermi level. It can be seen that the energy of two electrons paring by attractive interaction is always smaller than that of $2E_F$, the energy of two individual electrons. This pair is called the Cooper pair. Because Cooper pairs are bosons, they form a coherent many-body state, so called BCS ground state, by performing Bose-Einstein condensation below critical temperature.

In BCS theory, the interaction potential is given as a constant value regardless of direction. Therefore, the spatial part of the Cooper pair wave

function is isotropic (total orbital momentum L = 0). The spin state must be antisymmetric by Pauli's principle. Therefore, Cooper pair is described as $\{\vec{k}\uparrow, -\vec{k}\downarrow\}$. That is, a singlet with opposite momentum of two electrons. All elemental superconductors form these Cooper pairs. For complex materials with different symmetry interaction potentials, spin triplets can also occur.

In the case of a phonon-mediated superconductor, the size of the Cooper pair is about 10-100 nm. Since the electron density in the solid is about 10^{23} cm^{-3}, the number of Cooper pairs per unit volume is about 10^6. From this fact, it can be expected that the Cooper pair is inevitably overlapped. This makes it easy to know that a coherent quantum state is formed. According to the BCS theory, this is expressed by the following coherent factors [15]:

$$|v_{\vec{k}}|^2 = \frac{1}{2}\left(1 - \frac{\epsilon_{\vec{k}}}{\sqrt{\epsilon_{\vec{k}}^2 + \left|\Delta_{\vec{k}}\right|^2}}\right) \quad and \quad |u_{\vec{k}}|^2 = 1 - \left|v_{\vec{k}}\right|^2 \qquad (2)$$

This equation gives the probabilities of the state $|\vec{k}\uparrow; -\vec{k}\downarrow>$ being occupied or unoccupied, respectively. Even at T=0, occupation probability is smeared near Fermi level E_F (see Figure 1).

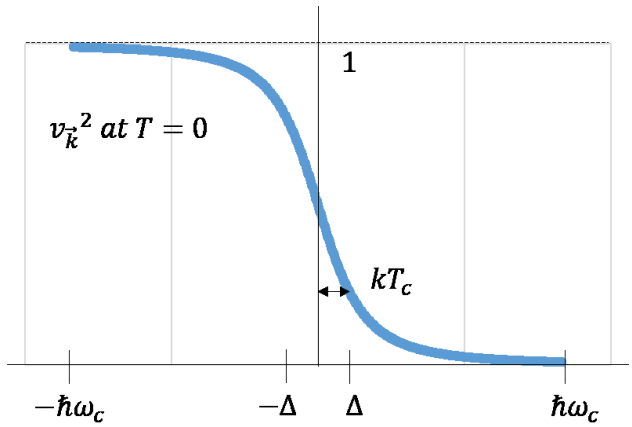

Figure 1 Plot of BCS occupation fraction

In Eq. 2, $\epsilon_{\vec{k}}$ is the single electron energy with respect to the Fermi level of the normal metal, $\Delta_{\vec{k}}$ is superconducting order parameter. It is described by the BCS gap function

$$\Delta_{\vec{k}} = -\sum V_{\vec{k},\vec{k}'}\Delta_{\vec{k}'}\frac{\tanh(E_{\vec{k}'}/2k_BT)}{2E_{\vec{k}'}}. \quad (3)$$

From BCS approximation that $\Delta_{\vec{k}} = \Delta$ and $V_{\vec{k},\vec{k}'} = -V$, Eq. 3 becomes

$$\frac{1}{V} = \frac{1}{2}\sum\frac{\tanh(E_{\vec{k}'}/2k_BT)}{E_{\vec{k}'}} \quad (4)$$

where $E_{\vec{k}'} = \sqrt{\epsilon_{\vec{k}}^2 + |\Delta_{\vec{k}}|^2}$.

The critical temperature T_c is the temperature at $\Delta_{\vec{k}} = \Delta \to 0$. After

changing the sum to an integral and using the symmetry of $\epsilon_{\vec{k}}$ about Fermi level, we can change Eq. 4 to the following equation.

$$\frac{1}{N(0)V} = \int_0^{\hbar\omega_c/2k_BT} \frac{\tanh x}{x} dx \tag{5}$$

This integral can be evaluated and yields the equation.

$$k_B T_c = 1.13\ \hbar\omega_c e^{-1/N(0)V_0} \tag{6}$$

Also in Eq. 3 at T = 0, we can get simple expression of gap function as follows.

$$\Delta(T=0) = 2\hbar\omega_c e^{-1/N(0)V_0} \tag{7}$$

Therefore, there exists a universal ratio of the gap value and the critical temperature.

$$\frac{2\Delta(0)}{k_B T_c} \approx 3.53 \tag{8}$$

So far, we have studied the Cooper pair and ground state of BCS theory [7], [15]. So what do you think of the excited state? The simplest excite state is when single unpaired electrons are generated in the BCS ground states. The single particle excitation generated in the superconductor is called a quasiparticle, which is an elementary excitation from a typical many-body ground state. The energy dispersion relation of this quasiparticle is derived from BCS theory and read as

$$E(\vec{k}) = \sqrt{\epsilon_{\vec{k}}^2 + \Delta^2} \quad with \quad \epsilon_{\vec{k}} = \frac{\hbar^2 k^2}{2m} - E_F \,. \tag{9}$$

Thus quasiparticle has a minimum energy Δ which describes and energy gap for excitation from the ground state. The corresponding density of states of quasiparticles in the superconducting state is given by

$$D_s(E) = D_n(0)\frac{|E|}{\sqrt{E^2-\Delta^2}}, \tag{10}$$

where $D_n(0)$ is the density of states in the normal state at Fermi level. $D_s(E)$ is zero for $E < |\Delta|$. And it diverges at $\pm\Delta$. The opening of an energy gap in the excitation spectrum is definitely one of the important results of BCS theory. This energy gap was observed experimentally in absorption spectroscopy using infrared light or ultrasound as well as specific heat measurement. However, the most direct method is quasiparticle tunneling spectroscopy.

1.1.3 Eliashberg Theory

All solids consist of atomic lattices. Since the lattices have thermal energy, they oscillate based on the equilibrium position. This oscillation causes electron scattering and appears as a resistance. From the viewpoint of scatting, this vibrational motion can be expressed as particles that collide with electrons. This is the phonon that represents the collective lattice vibration as a quasiparticle. By the second quantization, the quasiparticle is represented by a simple creation and annihilation operation, and for the

phonon it is given by [7]

$$H_{harm} = \sum_{\vec{q}} \sum_{j}^{3n} \hbar\omega_j(\vec{q})(b_{j,q}^{\dagger} b_{j,q} + \frac{1}{2}). \quad (11)$$

Eq. 11 describes a system of independent harmonic oscillators, whose energy dispersions are $\omega_j(\vec{q})$. For small momentum $\vec{q}$, if the dispersion of vibration mode is linear in q, it is called acoustic phonon. If it has non-zero energy at q = 0, it is called optical phonon.

For many kinds of physics analysis, full information of phonon dispersion relation $\omega_j(\vec{q})$ is not necessary. Many physics depend only on the energy of phonon mode not on their momentum. Therefore, it is enough to know how many phonons are there at specific energy. We call this phonon density of states $F(\omega)$, which is given by

$$F(\omega) = \frac{V}{N} \sum_{j} \frac{1}{(2\pi)^3} \int \frac{ds}{|\nabla_{\vec{q}} \omega_j(\vec{q})|}. \quad (12)$$

From integration, all directional information is lost. At some $\vec{q}$, $\nabla_{\vec{q}} \omega_j(\vec{q}) = 0$, which means dispersion is flat at q. According to Eq. 12, at this point the density of states diverge resulting in characteristic peaks so called van Hove singularities [9]. Because of acoustic phonon which has linear dispersion near q=0, low energy part of density of states is quadratic in energy.

Until now, we have only dealt with free phonons that do not have any

external interaction. By the Born-Oppenheimer approximation, electronic motion and atomic motion can be separated, because electron mass is far smaller than atomic mass. However, some correction to this approximation should be considered. The Fröhlich Hamiltonian for the electron-phonon interaction is as follows [7].

$$
\begin{aligned}
H_F &= \sum_{\vec{k}} \varepsilon(\vec{k}) c_{\vec{k}}^{\dagger} c_{\vec{k}} \\
&+ \sum_{\vec{q},j} \hbar\omega_j(\vec{q}) \left(b_{j,q}^{\dagger} b_{j,q} + \frac{1}{2} \right) \\
&+ \sum_{\vec{k},\vec{G}} \sum_{\vec{q},j} [M_j(\vec{q})\, c_{\vec{k}+\vec{q}+\vec{G}}^{\dagger} c_{\vec{k}} b_{\vec{q},j} + \\
&M_j(-\vec{q}) c_{\vec{k}-\vec{q}+\vec{G}}^{\dagger} c_{\vec{k}} b_{\vec{q},j}^{\dagger}]
\end{aligned}
\tag{13}
$$

While the first term in Eq. 13 refer to free electrons and the second term is for free phonons, the last third one describes the scattering of electron with wave vector $\vec{k}$ into $\vec{k}+\vec{q}$ absorbing (annihilation) a phonon of $\vec{q}$ or emitting (creating) one electron with $\vec{k}-\vec{q}$ and one phonon $\vec{q}$. This process is well expressed in Figure 2 [7].

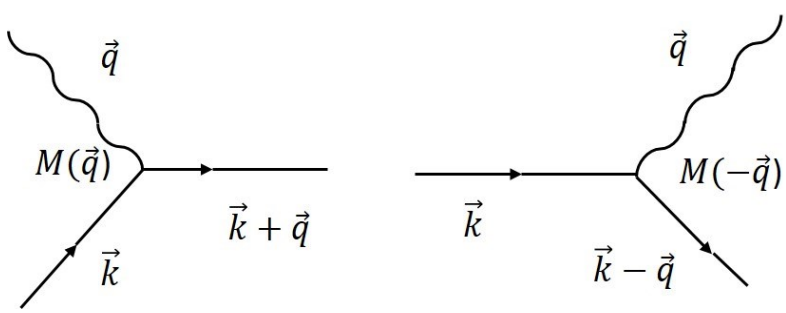

Figure 2 Feynman Diagrams of electron-phonon scattering

The phonon emitted by one electron can be absorbed by another electron. Therefore, it is easy to imagine transmitting electron-phonon interactions. This interaction can be attractive could be understood by considering the positively charged lattice ions induced by a fast passing electron. The other coming electron should be attracted to this charged ions.

Using a suitable canonical transformation we can write down the interaction term in Eq. 13 to a new form in which the phonon operators do not appear explicitly. That is given by [7]

$$H_{e-e} = \sum_{\vec{k},\vec{k'}} \sum_{\vec{q}} |M(\vec{q})|^2 \frac{\hbar\omega_{\vec{q}}}{(\varepsilon_{\vec{k}+\vec{q}} - \varepsilon_{\vec{k}})^2 - (\hbar\omega_{\vec{q}})^2} c^{\dagger}_{\vec{k'}+\vec{q}} c_{\vec{k'}} c^{\dagger}_{\vec{k}-\vec{q}} c_{\vec{k}} \qquad (14)$$

For clear expression only one branch of the dispersion relation is considered and umklapp processes ($\vec{G} \neq 0$) are neglected. Eq. 14 now describe the effective interaction between two electrons by the exchange of a phonon $\hbar\omega_{\vec{q}}$ as illustrated in Figure 3 [7].

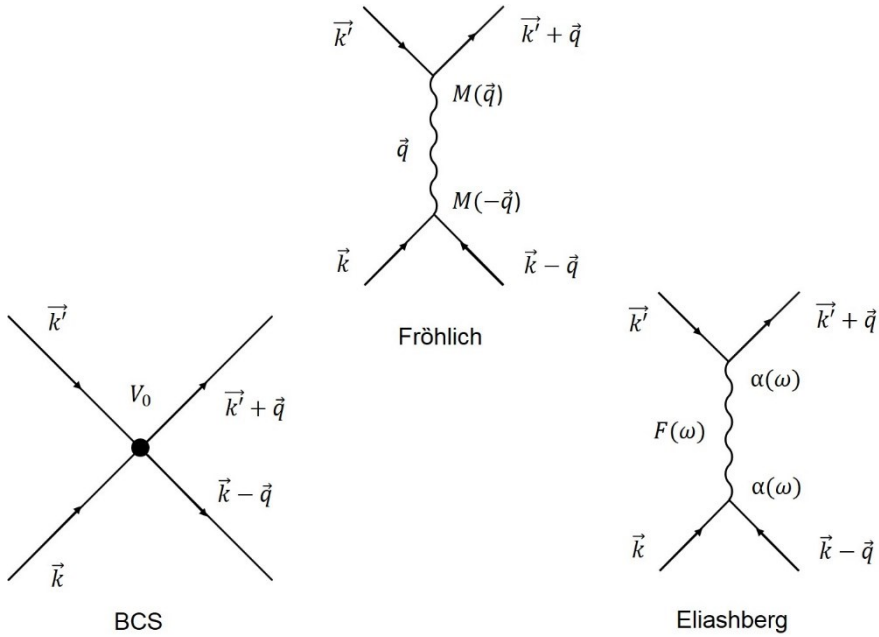

Figure 3 Illustration of electron-electron interaction in three different models

The new matrix term becomes negative if $\left|\varepsilon_{\vec{k}+\vec{q}}-\varepsilon_{\vec{k}}\right|<\hbar\omega_{\vec{q}}$. Thus the electron-electron interaction mediated to phonons becomes attractive near Fermi surface. BCS interaction potential is just the simplest approximation of Fröhlich's interaction.

$$|M(\vec{q})|^2\frac{\hbar\omega_{\vec{q}}}{\left(\varepsilon_{\vec{k}+\vec{q}}-\varepsilon_{\vec{k}}\right)^2-\left(\hbar\omega_{\vec{q}}\right)^2}$$

$$\rightarrow\begin{cases}-V_0, & if\ \left|\varepsilon_{\vec{k}+\vec{q}}-\varepsilon_{\vec{k}}\right|<\hbar\omega_D.\\ 0, & else.\end{cases} \tag{15}$$

The BCS theory explains a lot of experimental results especially in the weak-coupling regime $(D(E_F)V_0\ll 1)$, though it is a heavily simplified model.

The Eliashberg model (1960) is a bit closer to the Fröhlich model than the BCS model (Figure 3). The core physics of this theory is $\alpha^2F(\omega)$ and is called the Eliashberg function. This quantity is dimensionless and given by [7]

$$\alpha^2F(\omega) = \int \frac{d^2k}{v_F} \int \frac{d^2k'}{(2\pi)^3 v'_F} \sum_j M_j(\vec{k} - \vec{k'}) \delta(\omega - \omega_j(\vec{k} - \vec{k'}))(\int \frac{d^2k}{v_F})^{-1}. \quad (16)$$

In Eq. 16, $F(\omega)$ is the phonon density of states and $\alpha = \alpha(\omega)$ is the electron-phonon matrix element averaged over all phonons of energy $\hbar\omega$. Eliashberg theory also simplification version of Fröhlich model (Figure 3) which is not considering each polarization and each phonon momentum $\hbar\vec{q}$ dependence. However, it include not only the retardation and the spatial locality of interaction but also the true phonon density of states. It is an advanced form of the BCS theory. Superconducting properties are expressed by the Eliashberg gap equations [7] which are given as follows in zero temperature limit :

$$\Delta(\omega) = \frac{1}{Z_s(\omega)} \int_o^{\omega_c} d\nu \, Re(\frac{\Delta(\nu)}{\nu^2 - \Delta^2(\nu)})(K_+(\nu, \omega) - \mu^*) \quad (17)$$

$$(1 - Z_s(\omega))\omega = \int_o^{\infty} d\nu \, Re(\frac{\Delta(\nu)}{\nu^2 - \Delta^2(\nu)}) K_-(\nu, \omega) \quad (18)$$

This is a complex integral equations for the gap equation $\Delta(\omega)$ and

normalization factor $Z_s(\omega)$ which is related to the self-energy in the superconducting state. μ^* is an electron-electron pseudo-potential accounting for the screening. ω_c is the cut off frequency of the order $10\omega_D$. In this equations, the Eliashberg function is applied via

$$K_{\pm}(\nu,\omega) = \int_o^{\infty} d\omega'\, \alpha^2 F(\omega')\left(\frac{1}{\omega+\omega'+\nu+i\delta} \mp \frac{1}{\omega-\omega'-\nu+i\delta}\right) \tag{19}$$

From the Eliashberg function $\alpha^2 F(\omega')$ and the pseudo-potential μ^*, it is possible to derive the properties of phonon-mediated conventional superconductors, even in the strong electron-phonon coupling limit.

It is helpful to have a look on its simple example how to use this method. This calculation could be found in the paper written by Scalapino *et al*. [16] who solve the Eliashberg gap equations for a single phonon peak as depicted in Figure 4. In strong coupling regime, Schrieffer *et al.* proposed that the quasiparticle density of states should be given by

$$\frac{D_S(E)}{D_N(E_F)} = Re\left(\frac{E}{\sqrt{E^2-\Delta^2(E)}}\right). \tag{20}$$

According to the original BCS theory, the density of states has a form that smoothly decreases outside the gap. However, in terms of Eliashberg theory, the density of states shows deviation depicted in Figure 4 at the phonon energy ω_0 shifted by a gap Δ_0. There is a sharp decrease close to $\omega_0 + \Delta_0$.

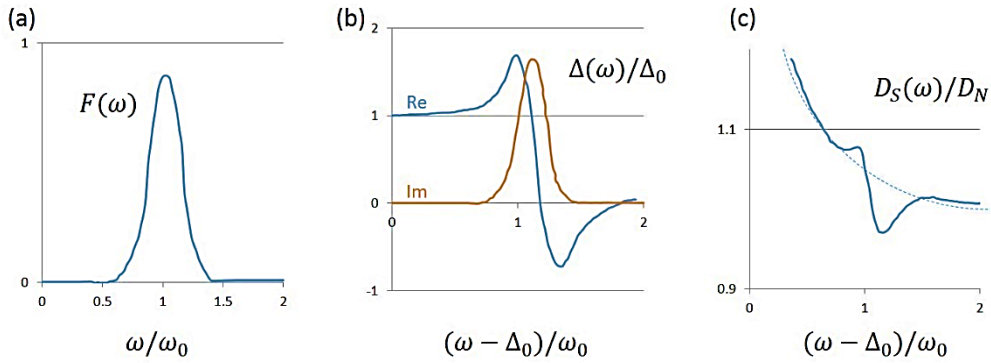

Figure 4 Application of the Eliashberg gap equations to a single-phonon peak model

(a) Single-peak phonon density of state $F(\omega)$. (b) Real and Imaginary part of gap parameter $\Delta(\omega)$. (c) The quasiparticle density of states : smoothly decaying curve from BCS theory and deviations from Eliashberg theory. Curves taken from [16]

We know electron-phonon interaction leads to a subtle change of the density of states. Therefore, there are also some deviation on the electronic band structure. In terms of many-body effect, “bare” electron energy dispersion $\varepsilon(\vec{k})$ has to be replaced by “dressed” electron energy dispersion $E(\vec{k})$, which is given by

$$E(\vec{k}) = \varepsilon(\vec{k}) + \Sigma(\vec{k}, E) \tag{21}$$

where $\Sigma(\vec{k}, E) = \Sigma_{Re}(\vec{k}, E) + \Sigma_{Im}(\vec{k}, E)$ is the self-energy account for the correction from the electron-phonon interactions. The electron-phonon interactions also exist on the normal metal such as Ag(111) [17]. There is one

kink near the Fermi level at $\pm\hbar\Omega_D$ labeled 1 in Figure 5.

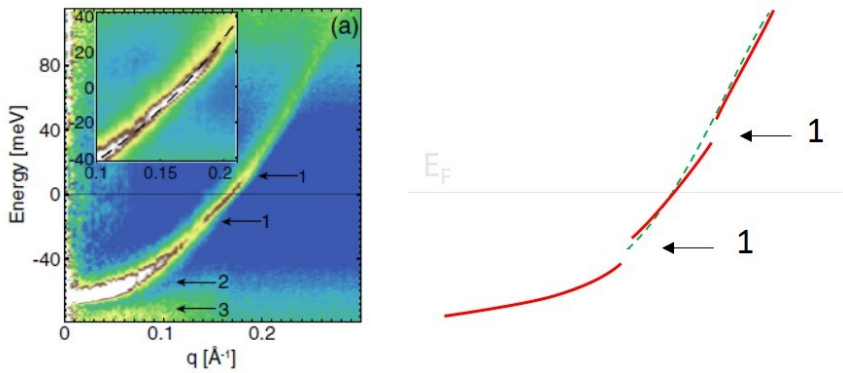

Figure 5 Energy dispersion curve with electron-phonon interaction on Ag(111)

: Image taken from **[17]**

So far, we have discussed how to describe the term of electron-phonon interaction more precisely. Many superconductors are explained by BCS theory, but in case of small bosonic peaks and dip appearing in DOS, Eliashberg theory should be introduced. Thus, the superconducting theory is being developed steadily to more precisely explain the physical phenomena from BCS to more sophisticated Eliashberg theory. According to Eliashberg theory, the superconducting critical temperature is 40K. In the next section, we will look at the fact that these predictions are clearly broken and the other kinds of superconductors.

1.2 Unconventional Superconductivity

Eliashberg theory evolved the concepts of BCS theory and extended it to

the strong coupling regime [18]. So many researchers would expect other superconductors to be explained based on the BCS theory. More they thought that the superconductivity phenomenon was explained in general. However, in 1986, J. G. Bednorz and K. A. Muller found superconductivity in a ceramic-based copper-oxide layer ($Ba_xLa_{5-x}Cu_5O_{5(3-y)}$) [3], bringing the superconducting system to a new phase. This discovery was revolutionary, firstly, that superconductivity appeared in ceramic-based insulating materials, and secondly that the electron-phonon coupling of BCS theory could not explain its critical temperature of 30K. Superconductivity was observed in other materials of the copper-oxide family, and the discovery continued, and the critical temperature reached 475K at present $Sn_{11}SbTe_{10}Ba_2VMg_{23}O_{46+}$ [19]. Since the critical temperature is higher than that of the elemental superconductor, they are called high-temperature superconductors.

Although high-temperature superconductors have not been described in the BCS theory and Eliashberg theory, researchers still agree that this unconventional superconductors will also exhibit superconductivity due to Cooper pairing. However, there are various hypotheses as to which bosonic mode other than phonon acts as a mediator of pairing. This situation is the same in heavy fermions discovered in 1979 [20] and in iron pnictides discovered in 2008 [4].

After the copper oxide series, another series of high-temperature superconductors began to be discovered, iron pnictides ($LaFeAsO_{1-x}F_x$, 2008 in Hosono group [4]). This discovery was also revolutionary because of iron. According to conventional superconductivity, the magnetic moment only serves to break superconductivity. In fact, superconductivity is broken when

a small amount of magnetic atoms are placed in a conventional superconductor. According to Eliashberg theory, $LaFeAsO_{1-x}F_x$ has a relatively small electron-phonon coupling constant and the expected Tc is only 0.8K. However, the actual measurement reached 26K. The discovery beyond this common sense and the impossibility of explaining it with existing theories was another opportunity for the scientific community to produce numerous theories and experiments with myriad discoveries and challenges.

The most promising scenario is Cooper pairing by spin fluctuation. The phase diagram of Fe pnictide shows antiferromagnetic or spin density wave in the absence of electron or hole doping. And as the magnetic phase disappears, the superconducting phase appears adjacent. In addition to this indirect evidence, one research supporting this scenario have been published [21]. They compared the optical measurement of $Ba(Fe_{1-x}Co_x)_2As_2$ with that of inelastic magnetic neutron scattering by Eliashberg theory, and found that the spin fluctuation is strongly coupled with the electron in that system.

Another difference between unconventional superconductors and conventional superconductors is the symmetry of order parameters. Conventional superconductors have isotropic s-wave gap symmetry because S = 0 and L = 0. As a result, we have the quasiparticle density of state of fully-gapped form of U-shape. However, Cuprate (coper-oxide) has d-wave symmetry because it is spin singlet (S = 0) and L = 2. Thus, since the gap symmetry is not isotropic and the quasiparticle density of state is represented as the average value in all k directions, it has a V-shape in this case. In the case of Fe-based superconductor, s + - symmetry is proposed

and verified through many experiments. The gap parameter is isotropic but the sign at the Gamma point and at the M point are different. Depending on whether the fermi surface passes through two pockets of different sign, it is either a V-shape gap or a U-shape gap.

Unconventional superconductors have been studied mainly in copper oxide series and Fe pnictide series. Many experiments and scenarios have emerged because existing theories do not fit well, but they implicitly agree that Cooper pairing will occur through other mechanisms.

1.3 Thin-film Superconductivity

In 1938, Shal'nikov first published thin-film superconductivity in Pb and Sn [22]. It is the first time to start the field of thin-film superconductors. The history of this field is closely related to that of material fabrication techniques, such as molecular beam epitaxy (MBE), pulsed laser deposition (PLD), thermal evaporation and sputtering of materials. In the early days before inventing MBE (1975), the most usual way to grow the 2D superconducting film were thermal evaporation and sputtering method. After evaporating superconducting material, the sample was quenched in ultrahigh vacuum by immersing in liquid helium. The resulting thin film was amorphous or granular with many disorders and random crystal orientations. This sample was used to study the basic properties of 2D superconductors. Since 1980, interest in quantum phase transitions (QPTs) has advanced to the study of QPTs in 2D thin-film superconductors, but the samples still had many disorders, amorphous and granular. Since 2000, material fabrication technologies such as MBE have been developed, making highly crystalline materials possible,

and the quality of samples has been improved day by day. At the same time, new superconductors such as Cuprate and Fe-pnictide have been discovered, enabling researchers to study 2D-limit physics in unconventional superconductors as well as conventional superconductors. Representative issues of 2D-physics in superconductors include localization of electrons and Cooper pairs, critical temperature with quantum size effect, Berezinskii-Kosterlitz-Thouless (BKT) transitions, and QPTs at zero temperature. The system studied is an interfacial superconductor such as $LaAlO_3/SrTiO_3(100)$, layered structure grown by MBE such as $FeSe/SrTiO_3(100)$, and mechanically exfoliated Cuprate such as $Bi_2Sr_2CaCu_2O_8$. In addition, the electric-field induced effect is studied by using the property of thin-film.

This thesis focuses on $FeSe/SrTiO_3(100)$ superconductors. We will examine how the $FeSe/SrTiO_3(100)$ grown, which tools were used, and what measurements were made in relation to the phonon and how these quantities relate to superconductivity. In addition, the discovery and simple physical properties of hexagonal phase FeSe other than the tetragonal phase FeSe that have been studied in the past will be discussed together.

Chapter 2. Scanning Tunneling Microscopy and Spectroscopy

In order to study phonon related physics in superconductor, many researchers used electron energy loss spectroscopy (EELS) or Helium atom scattering (HAS) method [23]. In order to investigate the low-dimensional superconductivity, we used a scanning tunneling microscope (STM). STM has the resolution up to the atomic size scale, so you can see the atomic structure and crystallinity of the grown crystal. In addition, local physical properties can be measured by tunneling spectroscopy. For example, local electron density of states (LDOS) and inelastic tunneling spectroscopy (IETS) can be measured by STM. Also, the electronic structure can be found by studying the quasiparticle interference patterns by Fourier transforming the conductance map. In this section, we will briefly introduce the STM and its application to measure the bosonic mode.

2.1 Principle of STM

A scanning tunneling microscope (STM) is consist of metallic tip, conducting sample and piezo-electric feedback scanner. Usually tip is sharp W, Pt/Ir, or Ir tip for non-magnetic experiment. However, for measuring magnetic signal, tip should have magnetism such as antiferromagnetic Cr tip or iron-coated W tip. The sharpness of tip apex is about 10 nm order by examining scanning electron microscope (SEM). The apex of the tip could be sharper by milling the end of the tip using focused ion beam (FIB). Conducting sample is usually

metal, semiconductor or superconductor. By STM, insulating materials could not be resolved, because of no conduction channels on them. Approaching tip to the sample is implemented by piezo-electric motor. There are two types of coarse approaching mechanism. The first one is Pan-style walking procedure [24]. The second one is Besocke-style [25]. After approaching tip and sample, fine feedback between tip and sample is necessary. It is realized by using piezo-electric scanner. This piezo-electric scanner carried out vertical feedback in sub pico-meter resolution by controlling tunneling current between tip and sample. Moreover, it is used to scan in lateral direction in sub Å resolution. By using scanning tunneling microscope, we can see the atomic structures and some physical properties of clean conducting surfaces.

2.1.1 Tunneling

Quantum mechanics has been established and various phenomena that are not possible in classical mechanics are possible. One phenomenon is "tunneling". Tunneling is a quantum mechanical conclusion that particles with small masses can pass over a larger energy barrier than their own. In the world of quantum mechanics, particles can simultaneously exhibit wave-like properties, and the particles can be described as wave functions. This wave is described as a simple oscillation function such as sine or cosine with a certain amplitude outside the energy barrier, and as an exponential function in which the amplitude is attenuated inside the energy barrier. As a result, the amplitude of this exponential term is non-zero even on the opposite side of the energy barrier, and consequently, particles exist in the form of waves

oscillating with the attenuated amplitude. Therefore, tunneling is a quantum mechanical phenomenon explained by the wave-particles duality.

There is a good example of the measurement using this tunneling phenomenon in the study on the superconductor. In 1960 I. Giaever measured the tunneling current in a sandwich structure of aluminum / aluminum oxide / lead. He also measured the BCS gap when the lead became a superconductor in the dI/dV curve [26]. After STM was invented, researchers are now able to measure the phenomena occurred at planar tunneling junctions also at local tunneling junctions. And also, this local probe can image the surface structure, so the effect of defect or impurity can be measured precisely.

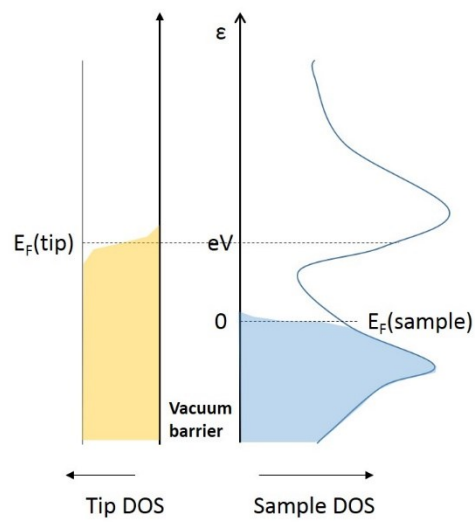

Figure 6 Schematic of tip-sample tunneling

Also, the tunneling current is the value obtained by integrating the local density of states of the sample where tip is located [27]. Let us now consider

how the tunneling current can be described physically by considering the density of states of tip and sample. If the bias voltage of + V is applied to the sample, the fermi level of the sample will be lower than the fermi level of the grounded tip as much as –eV (Figure 6). Let's describe the flow of electrons as an equation. First, the current flowing from the tip to the sample can be expressed as follows.

$$I_{t\to s}(\varepsilon) = -2\mathrm{e}\cdot\frac{2\pi}{\hbar}|M|^2\cdot\rho_t(\varepsilon-eV)f(\varepsilon-eV)\cdot\rho_s(\varepsilon)[1-f(\varepsilon)]$$
$$\rho_t(\varepsilon-eV)f(\varepsilon-eV): Filled\ tip\ satates\ for\ tunneling\ from \quad (22)$$
$$\rho_s(\varepsilon)[1-f(\varepsilon)]: Empty\ sample\ states\ for\ tunneling\ to$$

A dominant current flows from tip to sample for positive sample bias. However, there are also a small flow of electrons from sample to tip, given by

$$I_{s\to t}(\varepsilon) = -2\mathrm{e}\cdot\frac{2\pi}{\hbar}|M|^2\cdot\rho_s(\varepsilon)f(\varepsilon)\cdot\rho_t(\varepsilon-eV)[1-f(\varepsilon-eV)].$$
$$\rho_t(\varepsilon)f(\varepsilon): Filled\ sample\ satates\ for\ tunneling\ from \quad (23)$$
$$\rho_t(\varepsilon-eV)[1-f(\varepsilon-eV)]: Empty\ tip\ states\ for\ tunneling\ to$$

Summing these two flows and integrating over all energies ε, gives a net current from tip to sample as follows.

$$I_{t\to s}(\varepsilon) = -\frac{4\pi e}{\hbar}\int_{-\infty}^{\infty}|M|^2\rho_s(\varepsilon)\rho_t(\varepsilon-eV)\cdot[f(\varepsilon-eV)-f(\varepsilon)]\,d\varepsilon \quad (24)$$

This expression can be simplified at low temperature limit, because the Fermi function could be considered as sharp step function at this limit. For

example at 4.2K, the broadening of Fermi function is ~$2k_BT$ = 0.72 meV, which is sufficiently larger than superconducting gap in FeSe of 15 meV. In the approximation of perfect Fermi function, the tunneling current is

$$I_{t\to s}(\varepsilon) \approx -\frac{4\pi e}{\hbar}\int_0^{eV} |M|^2 \rho_s(\varepsilon)\rho_t(\varepsilon - eV)\, d\varepsilon. \tag{25}$$

The second simplification comes from the featureless DOS of tip near Fermi level. From this assumption the tunneling current formula becomes

$$I_{t\to s}(\varepsilon) \approx -\frac{4\pi e}{\hbar}\rho_t(0)\int_0^{eV} |M|^2 \rho_s(\varepsilon)\, d\varepsilon \tag{26}$$

The last simplification is Bardeen's approximation, that says the matrix element for tunneling will be virtually independent of the energy difference between the two sides of barrier. Therefore, we can write down as follows.

$$I_{t\to s}(\varepsilon) \approx -\frac{4\pi e}{\hbar}\rho_t(0)|M|^2\int_0^{eV} \rho_s(\varepsilon)\, d\varepsilon \tag{27}$$

If we assume s-wave tip, $|M|^2 = e^{-2kz}, k = \sqrt{2m\varphi/\hbar^2}$, where z is the tip-sample distance. In conclusion, the tunneling current is approximated by

$$I_{t\to s}(\varepsilon) \approx -\frac{4\pi e}{\hbar}\rho_t(0)\cdot e^{-kz}\int_0^{eV} \rho_s(\varepsilon)\, d\varepsilon \tag{28}$$

In the next section, we will briefly discuss how STM can look at surface structures as atomic resolution.

2.1.2 Topography

Initially, measurements using tunneling phenomena were performed mainly at junctions by thin oxide layer [28]. Then there was the concept of vacuum tunneling in the 1970s, and this concept was realized in 1982 when G. Binnig and H. Rohrer invented a scanning tunneling microscope (STM) [29]. STM is a microscope that operates by measuring and feed backing the electron flow tunneling the vacuum when the metal tip approaches the sample as described above. Tunneling current is given as a function of the distance between the tip and sample and the work function of the sample. In the case of metal, the work function is given as 4 eV. When the distance between the tip and sample approaches 1 Å, the tunneling current increases by 10 times. Tip can scan the surface of the sample through the piezoelectric transducers because the motion of the piezoelectric transducer can be controlled at the pico-meter level. Usually the z-piezo, which adjusts the tip-sample distance when scanning, feeds back a constant tunneling current, which is called the constant current mode. Tunneling current is not only a function of distance between tip and sample, but also a function of the surface's local density of states. Therefore, in the image obtained, the height information and the local electron density are inevitably mixed. From Eq. 28, the recorded tip height z is linear in the topography, but logarithmic in the integrated DOS. The STM's piezo-motor is designed to have a sub-pico meter resolution in the z direction and a sub-Å resolution in the x-y direction. Therefore, it is possible to study the physical properties at the atomic level.

2.1.3 Tunneling Spectroscopy

In addition to imaging the sample surface, STM can also reveal the local density of states (LDOS) on specific region of the sample, up to several eV from Fermi level in both filled states and unfilled states. This is realized by stopping feedback and maintaining tip-sample distance and then sweeping dI/dV as bias voltage. Tunneling conductance dI/dV appears to be proportional to the LDOS of the sample from Eq. 28.

$$\frac{dI}{dV} \approx -\frac{4\pi e^2}{\hbar} e^{-kz} \cdot \rho_t(0)\rho_s(eV) \tag{29}$$

To reduce noise, a lock-in technique used which is adding a small ac modulation to the dc bias voltage and getting the first harmonics matched to the frequency of modulation.

$$\begin{aligned} \mathrm{I(V} + \mathrm{A}\sin\omega t) &= \mathrm{I(V)} + \frac{dI}{dV}(V) \cdot A\sin\omega t + \frac{1}{2}\frac{d^2I}{dV^2}(V)(A\sin\omega t)^2 + \\ &\approx \mathrm{I(V)} + \frac{dI}{dV} \cdot A\sin\omega t + \frac{1}{2}\frac{d^2I}{dV^2} \cdot A^2\left(\frac{1-\cos 2\omega t}{2}\right) + \end{aligned} \tag{30}$$

From Eq. 30, we know that the oscillating term $\sin\omega t$ is thus proportional to the differential conductance dI/dV. Moreover, we also know that oscillating term $\cos 2\omega t$ is proportional to the second derivative of tunneling current. In the next section, we will describe how we take inelastic electron tunneling spectroscopy from d^2I/dV^2.

2.1.4 Inelastic Electron Tunneling Spectroscopy

Inelastic electron tunneling was first attempted in 1966 by R. C. Jaklevic and J. Lambe to observe very small changes in conductance while studying Al-oxide-Pb planar junctions [30]. They found about 1% change in conductance as the peak of the second derivative of tunneling current and concluded that this is the vibrational mode of the molecule contained in the barrier. In other words, the vibrational energy of the molecule opens the channel through which the tunneling electrons flow into the inelastic channel. Therefore, applying a voltage higher than the vibrational energy of this molecule increases the slope of tunneling current. And this makes upward step in conductance. Finally, it appears peak at the second derivative of tunneling current (Figure 7).

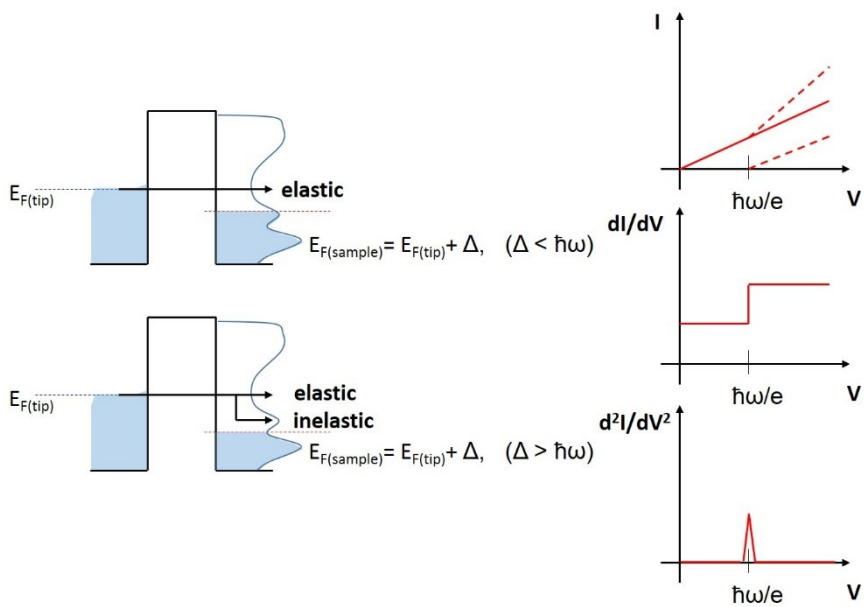

Figure 7 Inelastic Electron Tunneling Spectroscopy

2.2 Instrumentation

Before presenting the results of the experiment, we will first look at the equipment used here. This equipment was completed in the laboratory by students and professors' ideas and efforts from designing to assembling. The temperature can be lowered to 0.35K, and the magnetic field can be applied vertically by 9T and horizontally by 2T. In-situ sample growth and measurement is also possible because the scanner and sample preparation equipment are in an ultrahigh vacuum (UHV) chamber. Therefore, it is possible to measure the physical properties of uncontaminated samples. In this section, we will introduce and explain each part of this STM.

2.2.1 STM Scanner

First, let's look at the scanner part of STM. The STM scanner fabricated in the laboratory approaches a tip near to the sample with a Pan-type walker [24]. Because the sample is mounted on three tube piezo, coarse XY movement (less than ±0.5 mm) is possible. The specification of the scanner is that the maximum scan range is 440 x 440 nm^2 considering the maximum voltage of ±140V of the electronics used and in the 4.3 K, 1.58 nm/V in the XY direction and 0.5 nm/V in the Z direction. The CAD and photo of the Scanner are shown in Figure 8, Figure 9 and Figure 10.

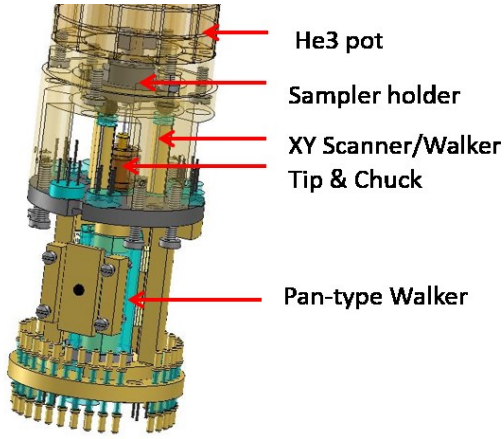

Figure 8 CAD of STM Scanner

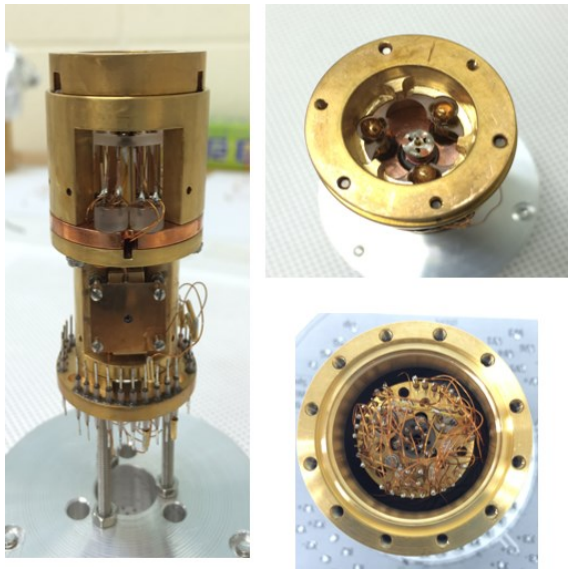

Figure 9 Pictures of STM Scanner

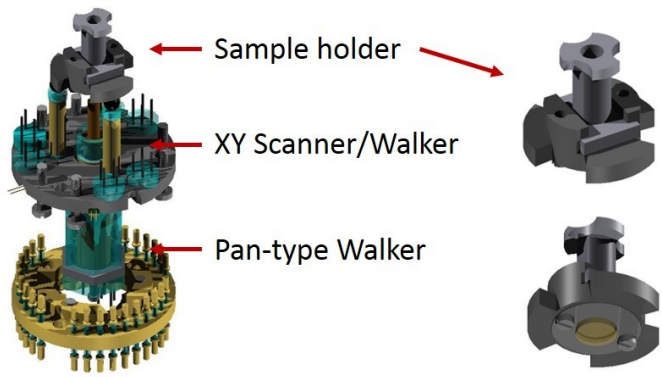

Figure 10 CAD of Scanner and Sample Holder

2.2.2 Ultrahigh Vacuum Chamber

This STM was installed inside an ultrahigh vacuum (UHV) chamber. This section discusses the UHV chamber. The fabricated chamber consists of a preparation chamber and main chamber (Figure 11). The preparation chamber is used for sample preparation and growth. And the main chamber is used for sample loading and scanning. In the preparation chamber, there is a sample heater for sample heating and annealing by e-beam and filament heating. And there is a tip heater for annealing and sputtering a tip. There is also an ion gun for sample sputtering. Finally, there is an assembly stage in which the prepared sample can be assembled with the sample chuck. There is also a carrousel storage that can store several samples and tips. The prepared sample with sample holder is assembled with the sample chuck, transferred to the main chamber by tray, and loaded on the scanner by vertical translator. Everything from preparation to experiment is done in vacuum (Figure 12 and Figure 13).

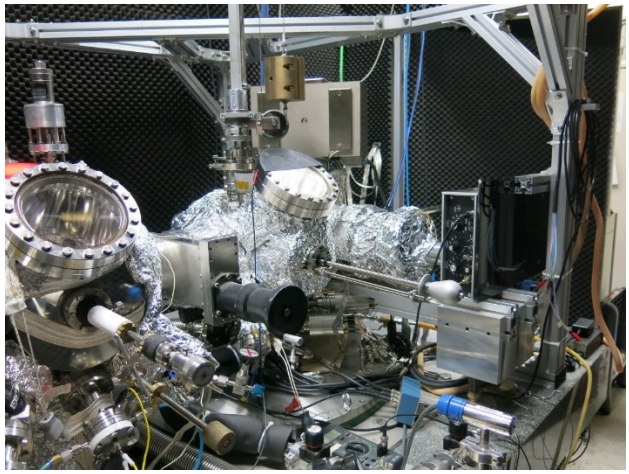

Figure 11 Preparation and Main UHV Chambers

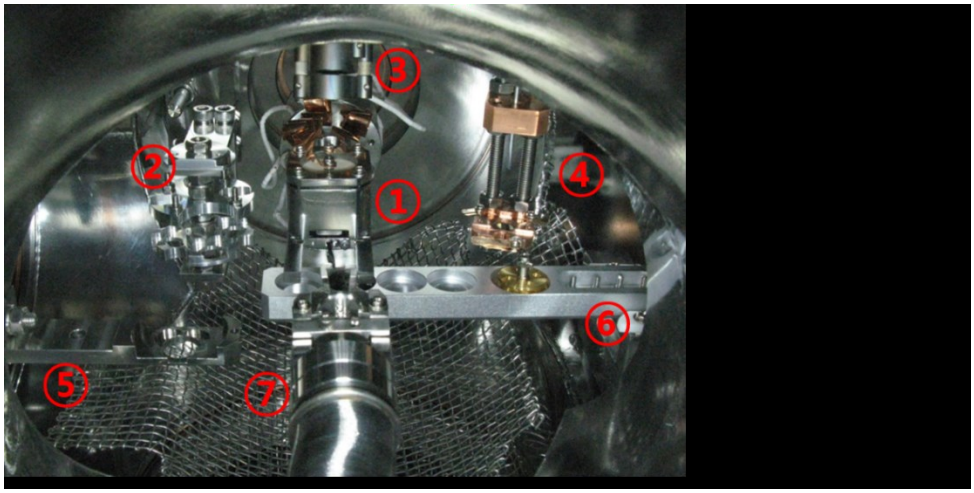

Figure 12 Inside of Preparation Chamber

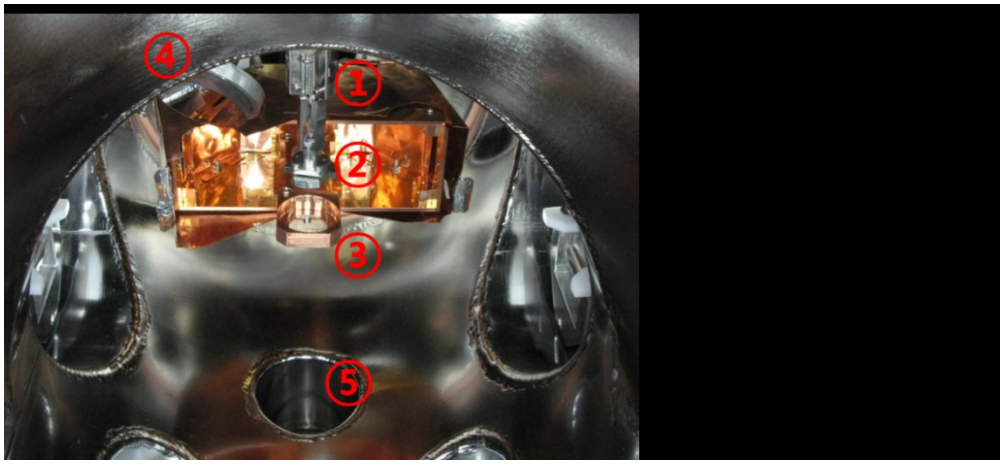

Figure 13 Inside of Main Chamber

2.2.3 He^3 Sorption Pumping System

The STM was also installed in a cryogenic insert capable of lowering the temperature to 0.3 K by He3 pumping. Therefore, the temperature can be lowered to 0.35K with STM scanner. The concept of the insert is shown in Figure 14. First, the needle valve is opened to allow the Liquid He4 to flow into the 1K pot. When the 1K pot is pumped by the rotary pump, the liquid He4 is vaporized and the temperature of 1K pot is lowered to 1.5K. Then, the He3 gas flowing around the insert is liquefied and becomes 1.5K liquid phase in the He3 pot. When this He3 is pumped by turning on the charcoal sorption pump, the temperature of He3 pot and STM scanner is lowered to 0.35K by super-cooling the liquid He3. The duration time of 0.35K is about 9 hours in this system.

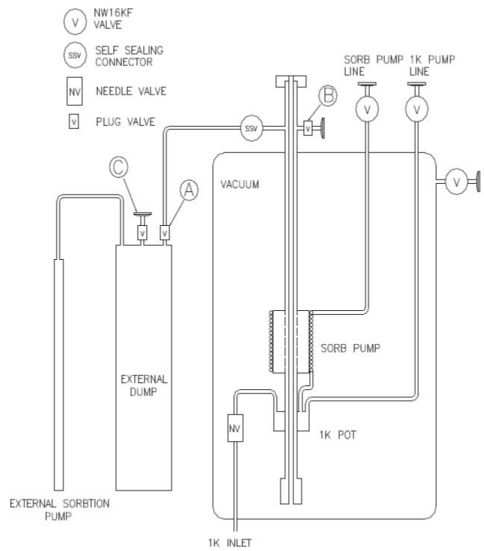

Figure 14 Schematic of He3 Insert

Chapter 3. STM Study of Surface Phonon on Cu_2O

3.1 Surface Phonon

3.1.1 Basic for Surface Phonon

Before considering the surface phonon, the general concept of phonon should be discussed. In a perfect single crystal, the atoms are arranged in a periodic lattice. Each atom can vibrate near the equilibrium position. This vibration is not independent but associative. Because this is a movement of atoms that are united with one another. Therefore, we call it collective vibration motion. Phenomenally, this collective motion causes a collision with electrons to create resistance. Physicists treat this collective motion as a scattering particle and call it a phonon.

The phonon can have two polarizations called longitudinal and transverse [9]. A longitudinal phonon is a phonon whose atomic oscillation and propagation direction coincide, and a transverse phonon is a phonon whose atomic oscillation and propagation direction are perpendicular. Moreover, there are two kinds of phonon. The first is an acoustic phonon, and the second is an optical phonon. The difference between acoustic phonons and optical phonons is that the movement of the atoms is in phase (acoustic branch) or out of phase (optical branch). If there is one atom in a unit cell, there are only acoustic phonon branches. However if there are several atoms in a unit cell, optical phonon branches appear.

In the study of lattice dynamics, we measure and calculate how the phonon energy varies with the wave vector k. The relationship between phonon

energy ω and phonon momentum k is called phonon dispersion $\omega(k)$. Usually, acoustic phonon has zero energy at zero momentum and linear dispersion near the zero momentum. However, optical phonon has non-zero energy at zero momentum [9].

Then, what is the surface phonon? It is the collective lattice vibration associated with surface [31]. And it arises on the termination of the perfect single crystal. There are two kinds of surface phonon. The first one is called as the resonance which appears in the bulk-phonon dispersion bands. The second is pure surface phonon which appears outside of the bulk-phonon bands. A particular mode called Rayleigh phonon exist across the entire Brillouin zone (BZ) and is known to have a linear dispersion curve near the Surface Brillouin zone (SBZ) center. Study of surface phonon gives information about the surface relaxation, type of defects on the surface, or other surface phonon mediated phenomena.

There are two traditional methods for measuring surface phonons. The first is Inelastic He atom scattering (HAS). The second is electron energy loss spectroscopy (EELS). HAS can measure the phonon dispersion with energy range 30-50 meV with resolution 0.5-1.0 meV [32]. EELS extend energy range up to 500 meV, but the resolution is about 7 meV [32]. Due to the recent development of STM technique, the surface phonon can be measured by inelastic electron tunneling spectroscopy (STM-IETS) at the tunneling junction [33], [34]. Using a local probe, it is possible to study the local effect of a particular impurity and surface stress, or correlation with other electrical properties. In next section, we introduce the experimental results obtaining by STM-IETS techniques.

3.1.2 Previous Measurement of STM-IETS

In 1998, Stipe *et al*. [35] was measured the vibrational spectroscopy of acetylene (C_2H_2) molecules isolated on Cu(100) using a STM local probe. In 1966, when Jaklevic *et al*. [30] measured the vibrational modes of molecules at the planar junction, in 1998 Stipe *et al*. measured the vibrational modes exactly on one molecule in the STM tip. This is the beginning of the STM-IETS. Then in 2004, Heinrich *et al*. [36] extended the STM-IETS technology to measure single-atom spin-flip spectroscopy. In this study, Heinrich measure the IETS due to the transition between Zeeman split states at Mn single atom on the insulating layer and metal surface. After that, STM-IETS succeeded in measuring the surface phonon mode of graphite [34], Au (111) and Cu (100) [33]. In other words, STM-IETS succeeded in measuring the IETS of single molecule [35] or single atom [36], but also succeeded in measuring surface phonons of conducting materials [33], [34]. In this experiment, we measured the surface phonon modes in 1ML copper oxide on Cu(100) and observed the change of the surface phonon modes at the step edge, that is the local line defect of the surface.

3.2 Surface Phonon Measured by STM-IETS

In this study, surface vibration mode was measured in 1ML copper oxide grown on Cu(100) by using STM-IETS. And I observe how the surface vibration mode changes by impurity or step edge. I extend the previous STM-IETS studies from measuring surface phonon modes [33], [34] to investigating the effect of surface imperfection on surface phonon.

3.2.1 Surface Structure of Copper Oxide

Given the importance of copper in the electronics industry, one can also see how important research in copper oxide is. The sample used in this study is Cu(100) (Figure 15). The study of copper oxide on Cu(100) has also been carried out extensively with numerous scientific instruments. In particular, LEED and STM were used to study the atomic structure of the surface [37]–[39]. In addition, studies on the surface vibrational mode have been carried out by measuring the absorption and reflection spectra through EELS [40]. This study measured the surface vibrational mode in copper oxide on Cu(100) using STM-IETS technique. Before discussing the measured surface vibrational modes, we first introduce the atomic structure of copper oxide.

Figure 15 Clean Cu(100) surface, 2V, 10pA

Copper oxide grown at low temperatures (400~500K) on Cu(100), studied by previous researchers [37]–[39], [41], may have two structures: the first one is a (2√2x√2)R45° reconstruction and begins to appear when the oxygen coverage is above 0.3 ML. The entire area is fully covered by

(2√2x√2)R45° reconstruction when the oxygen coverage is up to 0.5ML. And at this saturated structure, you can also find rectangular (2√2x√2)R45° islands. The (2√2x√2)R45° structure is very stable, flat and well-ordered. The atomic structure and surface vibration modes of this structure were measured by STM [37] and EELS [40], respectively. The second structure, called c(2x2), is a rough and not well-ordered as compared to the first one. However, Fujita's previous work [38] shows that oxygen atoms occupy the four-fold hollow-site of copper. Only the hollow-sites of copper were randomly filled with oxygen.

I will explain how to make these two copper oxide structures. Previous studies have shown that copper oxide grows when copper of 400-500 K is exposed to oxygen gas. The coverage is determined by the exposure time and oxygen pressure. It also determine the ratio of the two oxidized copper structures. In this study, Cu(100) was cleaned by sputtering and annealing for several cycles and then exposed to oxygen gas at 5 x 10^{-6} Torr for 10 minutes (3,000 L) while the heater was turned off and cooled at the final annealing temperature of 400°C. As a result, 0.4 mL of copper oxide was formed as shown in Figure 16.

The (2√2x√2)R45° reconstruction area and the c(2x2) area are present in Figure 16. In order to quantitatively analyze the roughness of the two regions, the profile across the two regions and one step was obtained as shown in Figure 17. In the profile, the step height is 180 pm, which is the same as that of Cu(100). Comparing the roughness of the two regions, the deviation of the roughness of the (2√2x√2)R45° reconstruction area is about 3 pm and that of the c(2 x 2) area is about 8 pm. As a result, it can be

seen that the previous research results are well reproduced in this study.

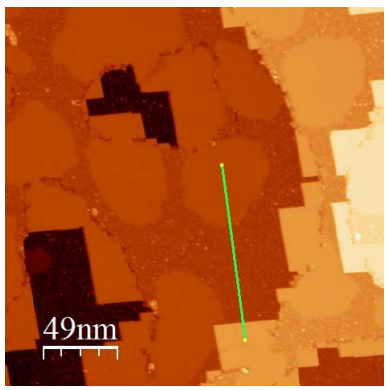

Figure 16 Copper oxide surface, 2V, 50pA

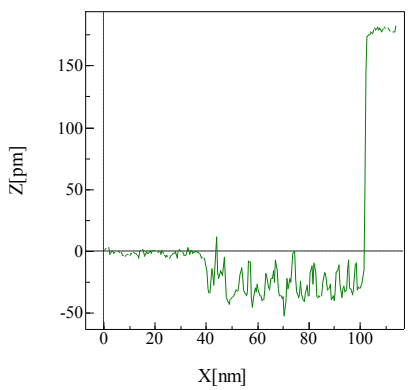

Figure 17 Profile across Copper oxide

Figure 18 is an enlarged topographic image. First, it can be seen that (2√2x√2)R45° structure is a well-ordered flat structure. It also shows that this structure has a certain nano size pattern. On the other hand, the c(2x2) structure appears to have randomly distributed oxygen atoms on specific sites of copper, as in the previous studies [38]. Figure 19 is a topographic

image of a sample at negative bias. The fact that the contrast in Figure 18 and Figure 19 is reversed reveals that (2√2x√2)R45° structure has higher density of states in positive bias than c(2x2) structure.

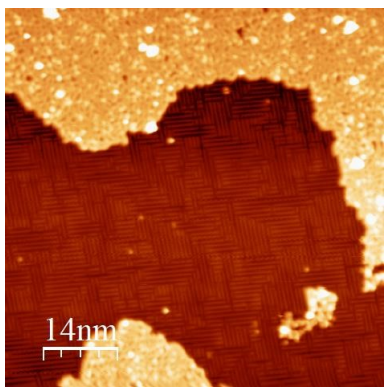

Figure 18 Copper oxide, 2V, 50pA

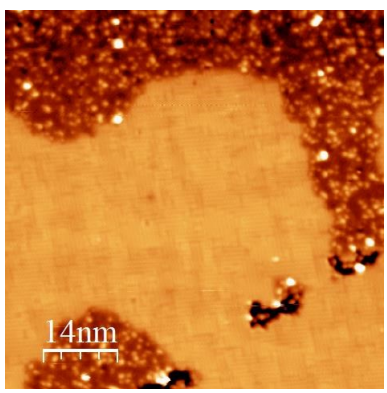

Figure 19 Copper oxide, -2V, 50pA

The atomic image of (2√2x√2)R45° structure is shown in Figure 20 and Figure 21. It is not a square but a rectangular. There is a case in which the resolution is improved far better by the absorbing an oxygen atom at the end of the tip. In this case, the atomic image of the (2√2x√2)R45° structure is well resolved in Figure 21. This image agrees well with the known structure [42]

in Figure 22.

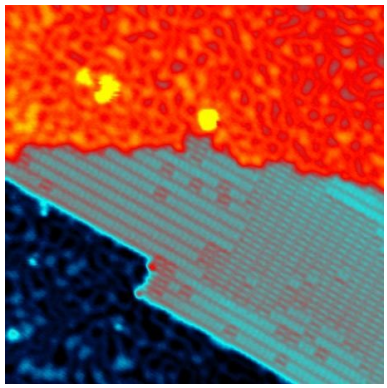

Figure 20 High Resolution Image of Copper Oxide, 1V, 50pA

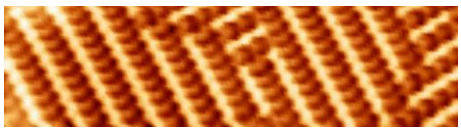

Figure 21 (2√2x√2)R45° Structure with Atomic Resolution

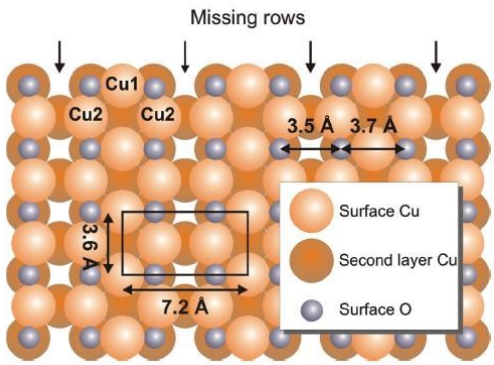

Figure 22 Schematic of Copper Oxide

Image taken from [42]

Previous studies have shown that (2√2x√2)R45° structure begins to form when θ = 0.3 ML and saturates at θ = 0.5 ML [37], [40]. In Figure 16 and Figure 20, (2√2x√2)R45° phase and c(2x2) phase coexist. However, when the oxygen dosing rate was increased over ~ 15,000 L, only (2√2x√2)R45° phase can be obtained. Figure 23 shows that there is only (2√2x√2)45° phase. And also there are many rectangular (2√2x√2)R45° islands on the surface with antiphase boundaries.

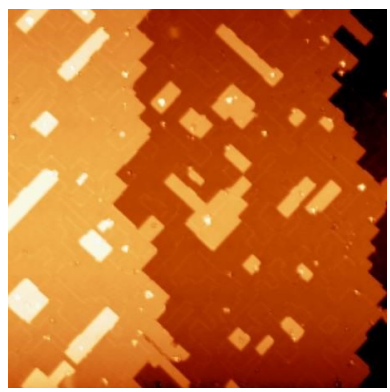

Figure 23 Copper oxide Islands

So far, I introduce how to grow copper oxide and show some images acquired by using STM. In terms of structure, two phases of (2√2x√2)R45° and c(2x2) agree well with the previous results and when the deposition rate increases, it saturates to a single phase of (2√2x√2)R45°. All experimental results reproduce the previous studies.

3.2.2 STM-IETS on Copper Oxide

In this section, surface vibration modes in two phases of copper oxide measured by STM-IETS are presented and compared with the vibration mode measured by EELS. Before then, surface phonon in clean Cu(100) should be discussed and the result is shown in Figure 24. The peaks and dips in Figure 24 are ±3.3 meV, +13.5 meV, -19.0 meV, and +27.5 meV. The surface phonon mode in Cu(100) is compared with the previous research results [43], [44] (Table 1). That is, 13.5 meV is the energy at the X point of the S_4 surface mode which is perpendicular to the surface and 27.5 meV is the energy at the M point of the S_6 surface mode which is parallel to the surface. And 19.0 meV is estimated to the energy at the M point of the S_1 or S_2 surface phonon mode. However 3.3 meV could not be explained as phonon modes on the zone-edge. This may be the acoustic phonon mode between Γ and the zone-edge, or vibrational mode of copper adatom on the tip apex [45].

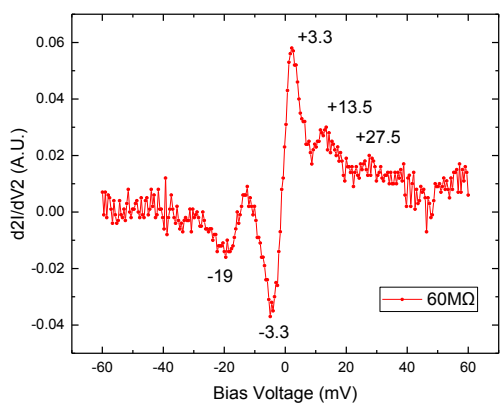

Figure 24 IETS on Cu(100)

		Theory	EELS	STM-IETS
$\bar{X}$	S_1(SH)	8.6 - 9.9	16.7	
	S_4(V)	12.4 – 14.6	13.2 – 13.4	13.5
	S_5(SH)	14.3 – 15.6		
	S_6(L)	24.1 – 27.0	25.2	27.5
$\bar{M}$	S_1(V)	16.4 - 18.7	16.7 – 17.0	19.0
	S_2(V)	20.0 - 22.3	20.3	
	(SH)	20.1 - 22.3		
	L_1(L)	20.1 – 22.3	20.4	
	S_6	26.9		

Table 1 IETS peaks on Cu(100) : unit in mV

On (2√2x√2)R45° phase, the surface vibrational mode measured by STM-IETS is shown in Figure 25. The temperature of the sample is about 6K and the modulation voltage applied during measurement is 3 mV, 5 mV, and 20 mV, from (a) to (c) respectively. The energy broadening by both temperature and modulation voltage is given by

$$\Delta \mathrm{E} = \sqrt{(5.4k_B T)^2 + (1.7eV_{mod})^2}. \quad (31)$$

The thermal broadening is 2.8 meV at 6K and the total energy broadening is 5.8 meV, 8.9 meV, and 34.1 meV when the modulation is applied at 3mV, 5mV, and 10mV, respectively. The STM-IETS peaks with

full width at half maximum (FWHM) and energy broadening obtained from Figure 25 are summarized in Table 2 IETS peaks on (2√2x√2)R45°.

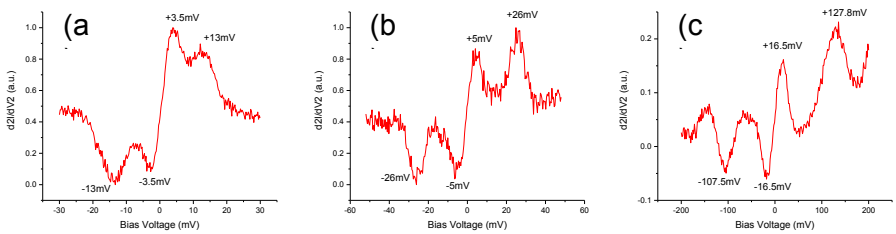

Figure 25 IETS peaks on (2√2x√2)R45°

STM-IETS Peak	FWHM	Broadening
3.5 mV	3.5 mV	5.8 mV
5 mV	6.2 mV	8.9 mV
13 mV	5.1 mV	5.8 mV
16.5 mV	25.0 mV	34.1 mV
26 mV	6.0 mV	8.9 mV

Table 2 IETS peaks on (2√2x√2)R45°

In order to find out the origin of the vibrational mode obtained from the STM-IETS in Table 2, we compare it with the previous EELS result [40]. The results obtained by STM-IETS are displayed on the surface vibration dispersion curves of (2√2x√2)R45° phase obtained through EELS (Figure 26). Compared with EELS, 3.5mV, 5mV, and 7mV peaks seem to correspond to

Rayleigh wave mode. For 13 mV peaks, Van Hove singularity at $\bar{M}$ point in Rayleigh wave mode or surface resonance mode at 90 cm^{-1} at $\bar{\Gamma}$ point. STM-IETS peak at 16.5 mV corresponds to surface resonance mode at 148 cm^{-1} at $\bar{\Gamma}$ point. The bosonic mode of 26 mV, which was not measured in the previous EELS study, has not yet confirmed its physical origin.

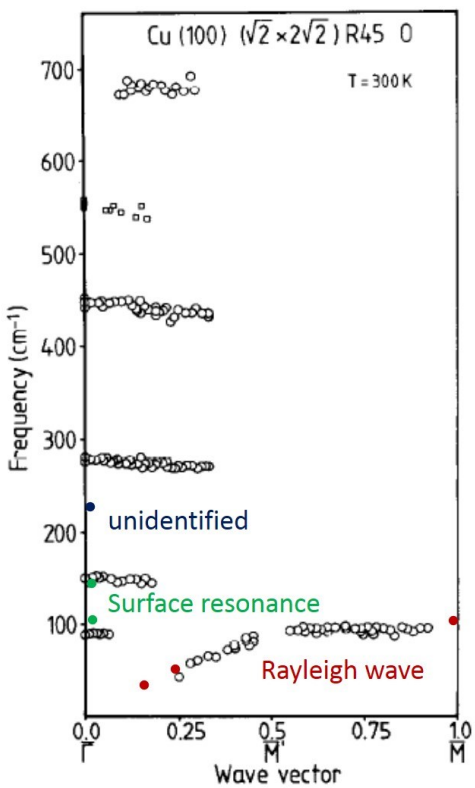

Figure 26 Surface Phonon of STM-IETS and EELS
Curves taken from [43]

Figure 27 shows STM-IETS results both in the c(2x2) phase and the (2√2x√2)R45° phase. IETS peaks on (2√2x√2)R45° phase differs from those on c(2x2) phase in that the magnitude of the IETS peak increases at 13 mV

and that the 8.5 mV peak of c(2 x 2) disappears and a 16.5 mV peak appears. Consider the physical origin of each peak. The peaks of 8.5 mV, 13 mV and 16.5 mV could be S_1 (surface horizontal), S_4 (perpendicular to surface) of the X branch, and S_1 (perpendicular to surface) mode of M branch of clean Cu (100) respectively (Table 1). Also, according to the previous EELS results [40], the modes corresponding to 13mV and 16.5mV is the surface vibrational mode by Cu lattice. The possible physical origins of the peaks and their variations are summarized in **Table 3**.

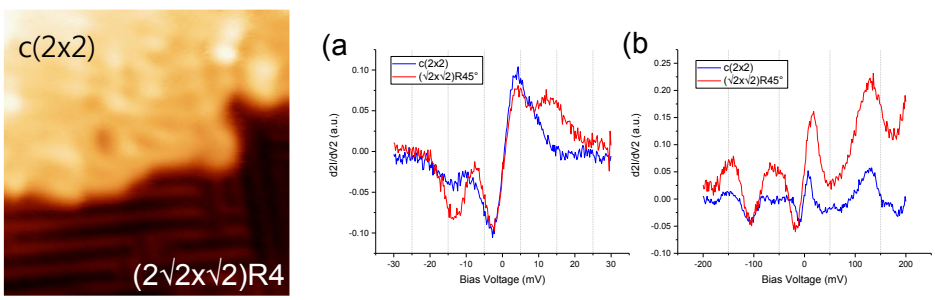

Figure 27 Comparison of IETS peaks between c(2x2) and (2√2x√2)R45°

Peak Energy	**Cu(100) Theory**	**c(2x2) EELS**	**(2√2x√2)R45° EELS**	**Cu(100) STM-IETS**	**c(2x2) STM-IETS**	**(2√2x√2)R45° STM-IETS**
8.5 mV	S_1(SH) at $\bar{X}$	none	none		shown	
13 mV	S_4(V) at $\bar{X}$	Cu surface resonance		shown	shown	shown
16.5 mV	S_1(V) at $\bar{M}$	not oxygen vibration				shown

Table 3 STM-IETS Comparison between c(2x2) and (2√2x√2)R45°

Each STM-IETS peak may not be a vibrational mode of adsorbed oxygen

from previous EELS research [40] and surface phonon calculation on Cu(100) [44]. Consider the reason that the mode of vibration by Cu is different at c(2x2) and (2√2x√2)R45°. c(2x2) does not significantly change the atomic structure of the Cu(100) surface, just has oxygen adsorbates on the surface. Oxygen atoms only give compressive stress on the surface [46]. According to surface phonon theory, compressive stress can red-shift the lattice vibrational mode. However, the shifted energy is estimated to be within mV and can therefore be ignored. Therefore, all original surface vibrational modes of Cu(100) should be similar on c(2x2) surface. 8.5mV and 13mV peaks could be the same peaks on clean Cu(100) surface which is S_1 and S_4 at $\overline{X}$ point. On the other hand, (2√2x√2)R45° is the case where the surface structure itself is changed because of Cu missing-row reconstruction. In this case, the surface vibrational mode itself should be recalculated. Of course, since the conventional Cu(100) structure is periodically changed, energy modes such as the original Cu(100) surface vibrational mode can survive. From this point of view, the enhancement of IETS peak at 13 mV is considered to be the effect of missing-row, and the fact that 8.5 mV peak disappears and 16.5 mV peak develops is interpreted in the same way.

In the previous section, we have observed the case where oxygen saturates whole surface which have only (2√2x√2)R45° terrace and islands. The STM-IETS was obtained across the step edge of the (2√2x√2)R45° islands. It is observed that the peak around +13 mV was enhanced at step edge (Figure 28, Figure 29). Why is this vibrational mode enhanced at step edge only for positive bias?

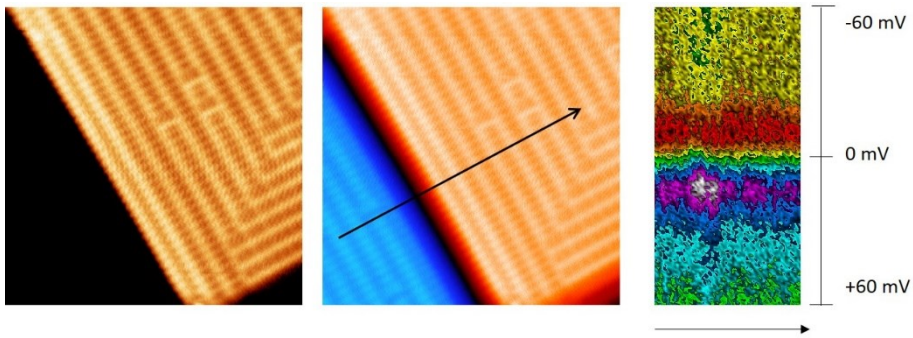

Figure 28 Spatial Resolved IETS across (2√2x√2)R45° step edge

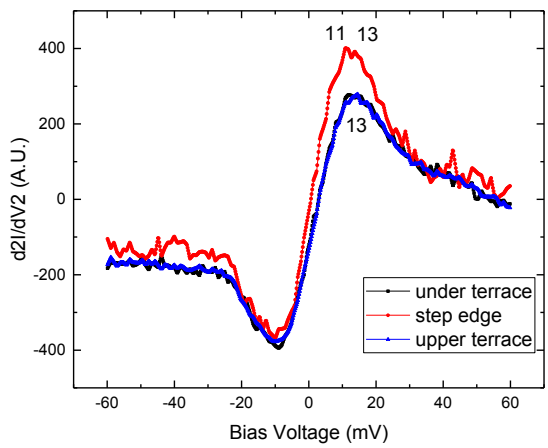

Figure 29 IETS on Terrace vs. Step Edge

Before answering this question, let's look briefly at how STM-IETS is theoretically explained [47]. When there is an adsorbate on the STM junction, the Hamiltonian is described as follows.

$$\mathrm{H} = \varepsilon_a(Q)c_a^{\dagger}c_a + \sum_k c_k^{\dagger}c_k + \sum_k (U_{ka}c_k^{\dagger}c_a + h.c.) \qquad (32)$$

$$+\varepsilon_t c_t^\dagger c_t + \sum_p \varepsilon_p c_p^\dagger c_p + \sum_p (U_{pt} c_p^\dagger c_t + h.c.)$$

After diagonalizing the electronic part of the Hamiltonian using one-particle eigenstates of adsorbate-metal $|\alpha>$ and of the tip $|\beta>$, the Hamiltonian can be reduced as

$$\begin{gathered} H = H_0 + H' \\ , H_0 = \sum_\alpha \varepsilon_\alpha c_\alpha^\dagger c_\alpha + \sum_\beta \varepsilon_\beta c_\beta^\dagger c_\beta + \hbar\Omega b^\dagger b \\ H' = \chi\left(b^\dagger + b\right) \sum_{\alpha,\alpha'} \langle\alpha|a\rangle\langle a|a'\rangle \, c_{\alpha'}^\dagger c_\alpha \\ + U_{at} \sum_{\alpha,\beta} (\langle t|\beta\rangle\langle\alpha|a\rangle \, c_\alpha^\dagger c_\beta + h.c.). \end{gathered} \tag{33}$$

From this Hamiltonian, inelastic tunneling could be described by

$$\begin{aligned} \frac{dI_{iets}}{dV} = \frac{4\pi e^2}{\hbar} \chi^2 |U_{at}|^2 \rho_t(E_F) \rho_a(E_F + \hbar\Omega \\ - \mathrm{eV}) \left| \int d\varepsilon' \frac{\rho_a(\varepsilon')}{\varepsilon' - E_F - eV} \right|^2 \Theta(eV - \hbar\Omega) \end{aligned} \tag{34}$$

, where $\varepsilon_a(Q) \approx \varepsilon_a(0) + \chi\left(b^\dagger + b\right)$ and $\chi = \varepsilon_a'(0) Q_0 = \varepsilon_a'(0)(\hbar/2m\Omega)^{1/2}$. From Eq. 34, STM-IETS peak intensity is proportional to the local electron density of states (LDOS) on the surface at the vibrational energy. In **Figure 28**, electron density of step edge is brighter than that of normal terrace. And from **Figure 30**, LDOS of the step edge is higher than that of terrace at +13 mV. However, at -13 mV LDOS of the step edge and that of terrace is almost same. Therefore, it can be explained that IETS is enhanced at + 13 mV from previous simple picture.

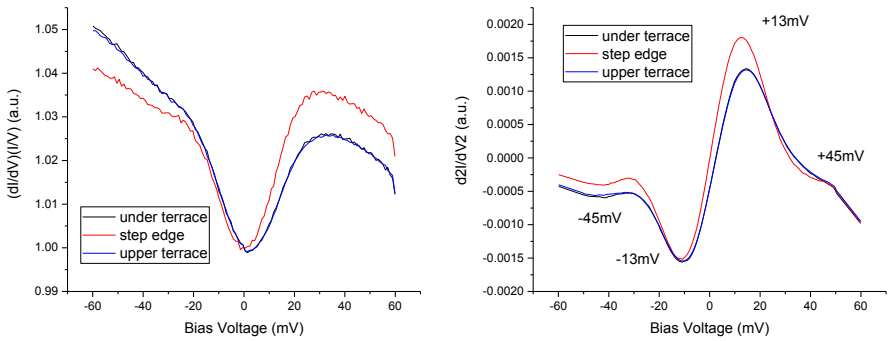

Figure 30 Spectroscopy and Numerical IETS across (2√2x√2)R45° step edge

Chapter 4. STM Study of tetragonal FeSe on SrTiO3(100)

4.1 Introduction

FeSe is the most simple Fe based superconductor. The first element Fe forming FeSe is transition metal with atomic number 26 and the electronic configuration is $[Ar]3d^6 4s^2$. It is chemically bonded mainly in the ionic state of Fe^{3+} or Fe^{2+}. The spin of the Fe atom is S = 2, and the bulk Fe is a ferromagnetic material. The second element Se forming FeSe is atomic number 34 and is nonmetal belonging to groups such as oxygen and sulfur. It is a simple monoclinic solid and diamagnetism. Fe and Se are combined to form FeSe in various phases. The phase to be introduced in this chapter is the tetragonal phase with PbO-structure (Figure 31). When Se is slightly less than Fe, it becomes a superconductor and the critical temperature is about Tc ~ 8K. The lattice constant of $FeSe_{0.88}$ is a = 3.77 Å, c = 5.50 Å [48]. Figure 32 is the phase diagram of FeSe. When the pressure is applied, the critical temperature increases up to 40K. More interesting, however, is that the critical temperature increases to over 60K when grown on SrTiO films [49]. As a result of this research, the interfacial effects of superconducting phenomena have been studied and attempts have been made to make superconductors with higher critical temperature by stacking thin-film superconductors.

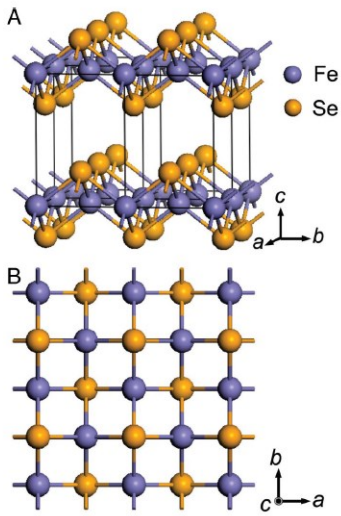

Figure 31 Structure of tetragonal FeSe

Image taken from [48]

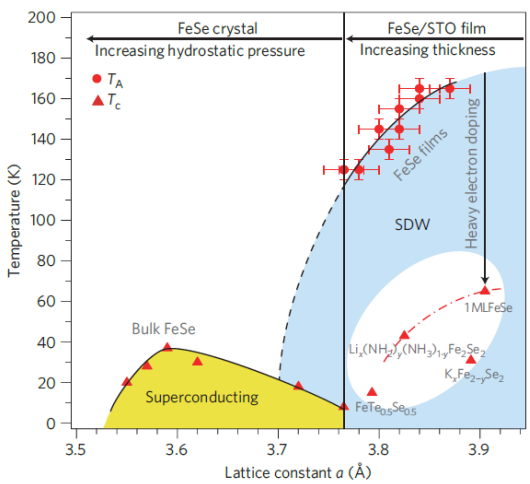

Figure 32 Phase Diagram of tetragonal FeSe

Image taken from [49]

4.1.1 Superconductivity on FeSe : From 3D to 2D

Bulk FeSe has been studied as the simplest Fe based superconductor, and its properties have been studied extensively. Particularly as the cleaving technique developed, surface studies of layered materials began to take place in STM study and the surface of many unconventional superconductors with layered structures began to be uncovered. Cleaved FeSe surface studies were also performed by T. Hanaguri (2010) [50]. In this study, Hanaguri obtained the quasiparticle interference pattern (QPI) on the cleaved FeSe surface and verified that the s± wave symmetry deduced by the APRES study is correct. Thereafter, attempts were made to combine MBE and STM to study thin-film superconductivity. Finally, the simplest FeSe was grown on a bilayer graphene on a SiC (0001) substrate to measure how superconductivity varies with thickness [51]. According to this study, superconductivity begins to appear from 2 triple-layer (TL) and converges to Tc = 8K, the critical temperature of bulk FeSe, at 8 TL. As such, FeSe research has progressed from bulk property research to thin-film research, driven by advances in cleaving and MBE technology.

4.1.2 Monolayer FeSe on SrTiO3(100)

As FeSe research was combined with MBE-STM, FeSe was also grown on $SrTiO_3$, a substrate where many cuprates were grown. And finally, surprisingly, the size of the superconducting gap on 1 ML FeSe/STO(100), obtained by STM, has increased by an order of magnitude over the superconducting gap obtained from bulk FeSe [2]. It has been repeated that

in-situ 4-probe measurements have shown that the critical temperature can reach T_c = 60-100 K [52]. Numerous researchers have begun to study 1 ML FeSe to reveal the T_c change mechanism of this superconductor due to the interface. And the facts revealed for the 1 ML FeSe/STO (100) system until 2017 are as follows [53].

1. **Critical Temperature**
   Critical temperature is T_c = 60 ~ 100 K from in-situ STM, ARPES, 4-probe studies.

2. **Interface structure between FeSe and $SrTiO_3$(100)**
   $SrTiO_3$(100) surface reconstruction maybe not important, but vertical structure of interface maybe the key. Double-TiO_x termination is imaged by cross-sectional TEM at the interface of FeTe/1ML FeSe/$SrTiO_3$(100).

3. **Electronic Structure**
   From STM-QPI result, electronic structure should be plain s-wave symmetry or “incipient” s+- symmetry.

4. **Pairing Mechanism**
   Phonon mediated Cooper paring may be dominated. But we do not exactly know which phonon mode is taken part in this pairing.

Thus, many studies on 1ML FeSe / SrTiO3 (100) have been conducted and many facts have been revealed. However, there is still a question of what phonon mode plays a major role in Cooper paring, and whether there are related bosonic modes other than phonons. In this study, STM-IETS

measurements were performed and analyzed using Eliashberg model.

4.2 Experimental Results

4.2.1 Superconductivity and Growth Condition

In this section, we will discuss superconductivity of tetragonal FeSe in terms of the growth condition. When certain conditions are satisfied, tetragonal FeSe exhibits superconductivity. I investigated the conditions under which the superconducting FeSe grows. Two of the most important growth conditions are the ratio of iron to selenium and post-annealing temperature [54]. The tetragonal phase grow when the Se/Fe deposition ratio is 5 ~ 30 [53]. When Fe is deposited more than Se, the hexagonal phase grows. The discussion of hexagonal phase will be in the next chapter.

The sub-ML tetragonal FeSe is grown as shown in Figure 33. It can be seen that FeSe grows into rectangular islands on $SrTiO_3$(100). Figure 33 shows the result of obtaining an atomic image in an arbitrary island. It can be seen that the FeSe islands grow well in tetragonal phase. Spectroscopy was performed on two different islands. As a result, peaks known as quantum confinement states as shown in Figure 34 were observed. This quantum confinement means that the FeSe island is electrically isolated from $SrTiO_3$(100) or that there is a potential barrier between FeSe and $SrTiO_3$. That is, FeSe and $SrTiO_3$ are considered to be decoupled electrically.

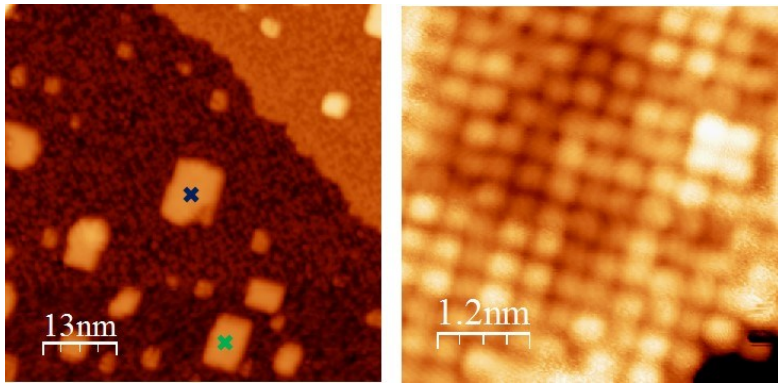

Figure 33 Sub Monolayer tet-FeSe/STO(100)

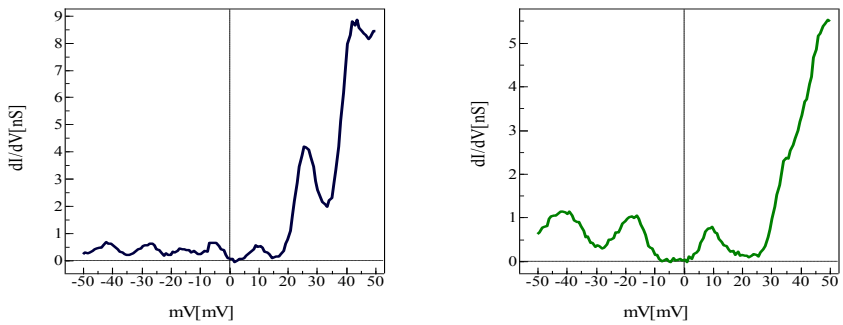

Figure 34 Spectroscopy of tet-FeSe islands

Figure 35, Figure 36, and Figure 37 show the images and spectroscopies of 1 ML FeSe grown on $SrTiO_3$(100). 1 ML FeSe is not always a superconductor. Post-annealing is an important parameter. When the post-annealing time is fixed to 2 hours, superconductor is not formed when the annealing temperature is lower than 550 ℃ (Figure 35, Figure 36), and superconductivity is obtained when the post-annealing temperature is about

570 ℃. Studies related to the post-annealing have already been performed by Li *et al.* [54] and the results are consistent with mine.

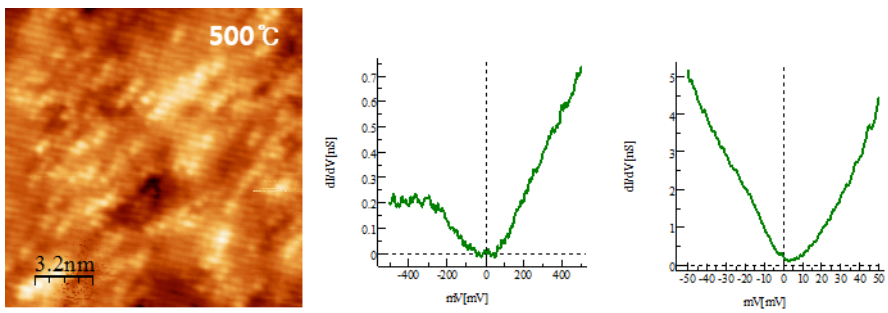

Figure 35 Topography and Spectroscopy of tet-FeSe, annealing ~500℃

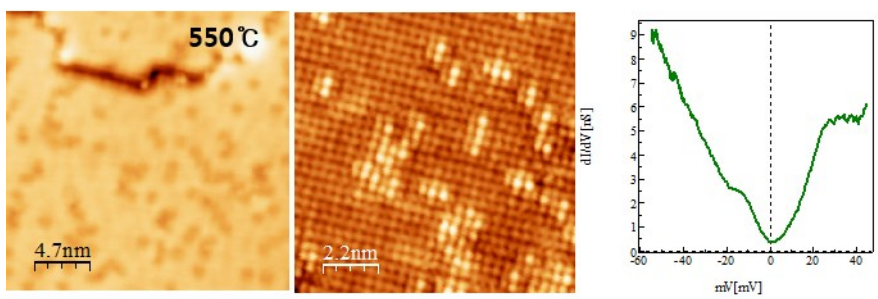

Figure 36 Topography and Spectroscopy of tet-FeSe, annealing ~550℃

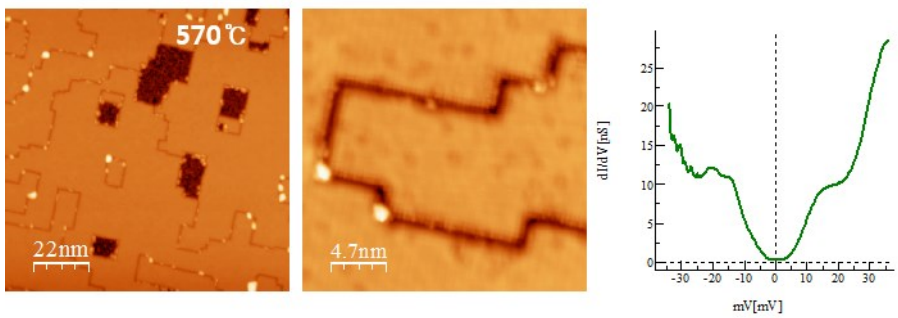

Figure 37 Topography and Spectroscopy of tet-FeSe, annealing ~570℃

4.2.2 Electronic Structure and Symmetry

In this section, I will discuss the electronic structure of tetragonal FeSe. Especially, we analyze the quasi-particle interference (QPI) pattern by Fast Fourier Transform (FFT) and discuss the symmetry of the electronic structure of FeSe. STM-QPI studies have shown that 1ML tetragonal FeSe on STO (100) has a plain s-wave symmetry on electronic structure [55]. The grown tetragonal FeSe was grown by co-deposition of Fe and Se at 600 ℃. The domain boundary was not the right angle but irregular and winding differently from the FeSe of Xue's group where the domain boundary had the right angle [2]. Of course, having a 2 × 1 reconstruction, a tetragonal phase, and having superconductivity are consistent with FeSe of the Xue's group. In this study, I reproduce the growth condition of Xue's group to grow tetragonal FeSe with righ angle domain boundaries. After confirming that the domain boundary in the FeSe is the right angle and having a superconducting gap, let's take a look at whether this FeSe has the same QPI and the same electronic

structure. The results are shown in Figure 38. Considering the QPI pattern, it is slightly different from the previous QPI pattern [55] in which 9 circles appear in the original 3 × 3 patterns. The q_2 circles are enhanced, and yellow dotted circle appears. (Figure 39).

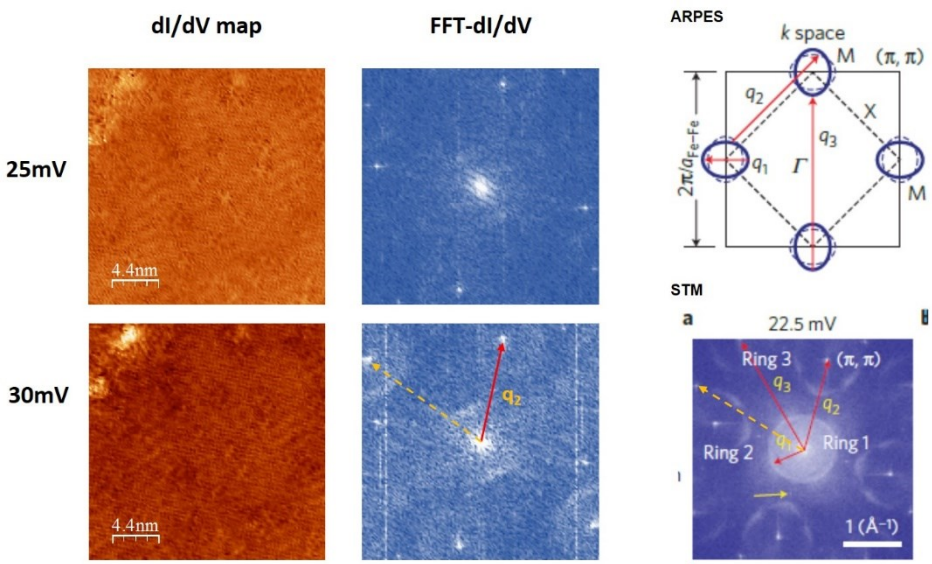

Figure 38 STM-QPI on tet-FeSe/STO(100) and Schematic of Electronic Structure on k-space

Schematic of k-space and gray STM-QPI taken from [55], [56]

I thought about why new circles appear and only q_2 circle appear as Figure 39. A comparison of the samples from the previous study and the samples from this experiment is shown in Figure 40. The sample used in the previous study has a wavy domain boundary in the measurement area, so that the scattering from the boundary can be dispersed in an isotropic direction. On the other hand, the sample used in this study has domain boundaries aligned

in one direction. Therefore, the scattering direction could be anisotropic. For this reason, only q_2 scattering appears in Figure 39. Studies on STM-QPI patterns by anisotropic scattering have been performed previously [56]. However, I cannot explain the other dotted circle. The plain s-wave picture cannot account for this dotted circle. Further analysis is required in the future.

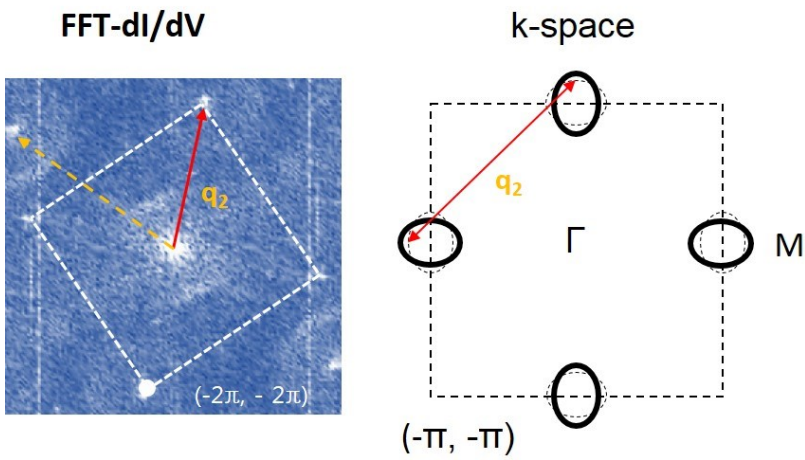

Figure 39 Anisotropic QPI patterns on tet-FeSe/STO(100)

gray STM-QPI taken from [56]

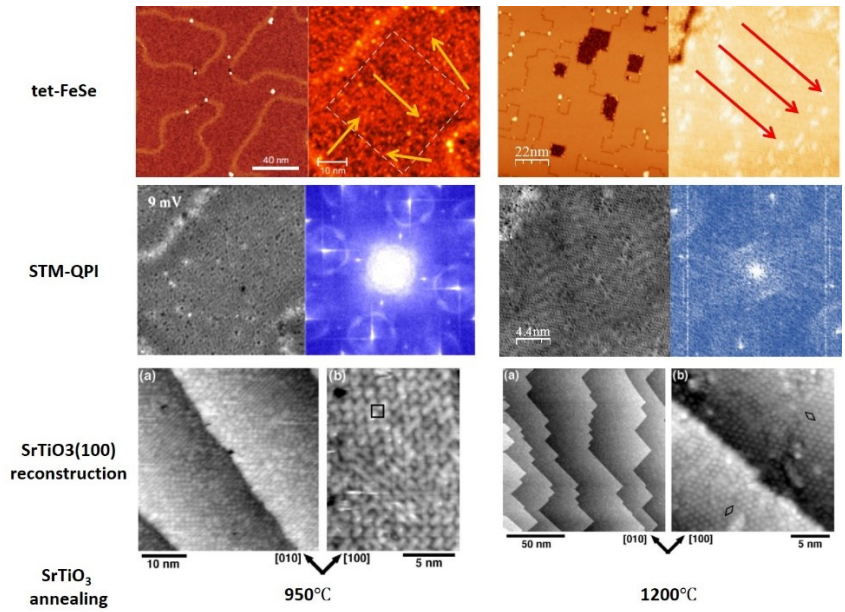

Figure 40 Comparison of anisotropic and isotropic STM-QPI

Bottom images taken from [55]

4.2.3 Phase Diagram

In this section, I will discuss how the phase of FeSe change with the carrier concentration. According to the previous researches [57], [58], the more the annealing of FeSe, the more Se deficiency and it makes the electron doping effect on FeSe. According to the ARPES study [58], FeSe undergoes a phase transition from the insulating to the superconducting phase when electron doping becomes large and the carrier density of Fe is about 0.1. In this STM study, we also observed that when the annealing was insufficient, the insulating tetragonal phase grew and the superconducting phase grew if annealing was sufficient. This result was introduced in Section 4.2.1.

Sometimes, growth of FeSe led to the growth of the √5x√5 phase Fe_4Se_5 (Figure 41), not the tetragonal 1x1 phase, which is considered to be an antiferromagnetic phase [59]. The phase diagram proposed in this study is shown in Figure 42.

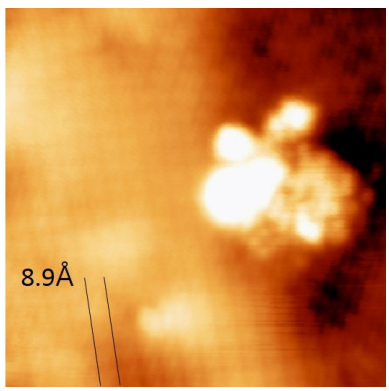

Figure 41 √5x√5 phase FeSe

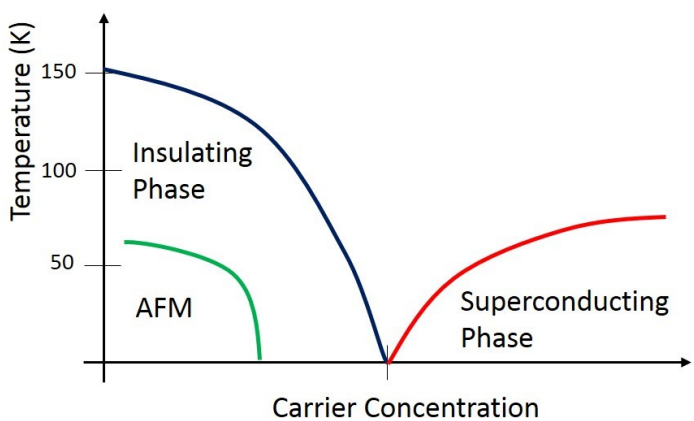

Figure 42 Phase Diagram of FeSe

4.2.4 Bosonic Modes

Since the emergence of high-temperature superconductors, many researchers have found that high-temperature superconductors are not described in the original BCS theory, and that new theories are needed. However, most researchers still agree with the proposition that high-temperature superconductors, like existing superconductors, have the root cause of the Cooper pair formed by the inter-electron attraction generated by certain bosonic modes. Therefore, a study of what bosonic mode is involved in forming this Cooper pair is an important study that reveals the origin of paring glue. In isotropic superconductors, bosonic mode was introduced in Chap. 1 as Eliashberg feature on spectroscopy. In other words, by analyzing the Eliashberg feature on the spectroscopy, we can see the energy of the bosonic mode that mediates the Cooper pair, and this energy is a clue to revealing the origin of bosonic mode.

Figure 43 and Figure 44 show low energy spectroscopy and high energy spectroscopies on tetragonal FeSe. Eliashberg features appeared on every spectroscopies. I have estimated by analyzing the energy that each Eliashberg feature points to which bosonic mode. As a result, the bosonic mode found in low energy spectroscopy is assumed to be acoustic phonon mode of FeSe [60] or spin fluctuation related mode. Whether this bosonic mode has a magnetic origin will be clarified later by another experiment by applying a magnetic field. The bosonic modes found in high energy spectroscopies are estimated to be phonon modes of both FeSe and $SrTiO_3$ [60]. The surface phonon mode of the $SrTiO_3$ and the optical phonon mode of the FeSe itself, which were specified in the previous EELS study [60],

were measured and a new bosonic mode, which is estimated to be another phonon mode of the $SrTiO_3$ [61], also appeared. The previous EELS study [60] and the ARPES studies [62] support the situation in which the $SrTiO_3$ surface phonon mode of the 92 meV is strongly claimed as a paring glue. However the relationship between the superconductivity and the 92meV phonon mode has not been proven in previous studies. In this study this is proved through the Eliashberg features on STM spectroscopies. In addition, I have experimentally found that other bosonic modes such as acoustic and optical phonon mode of FeSe, other surface phonon mode of $SrTiO_3$ also take part in pairing mechanism.

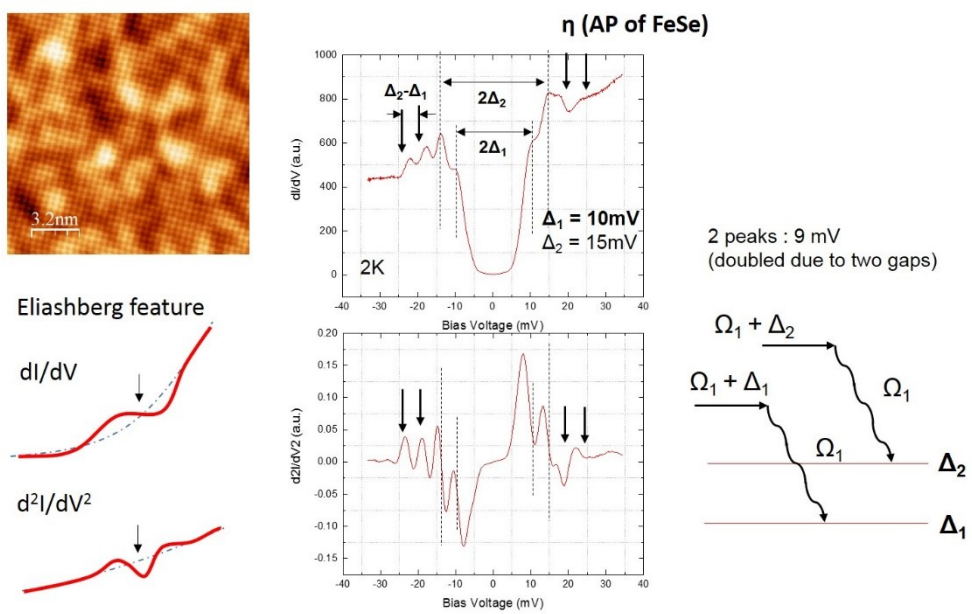

Figure 43 Low Energy Spectroscopy with Eliashberg feature

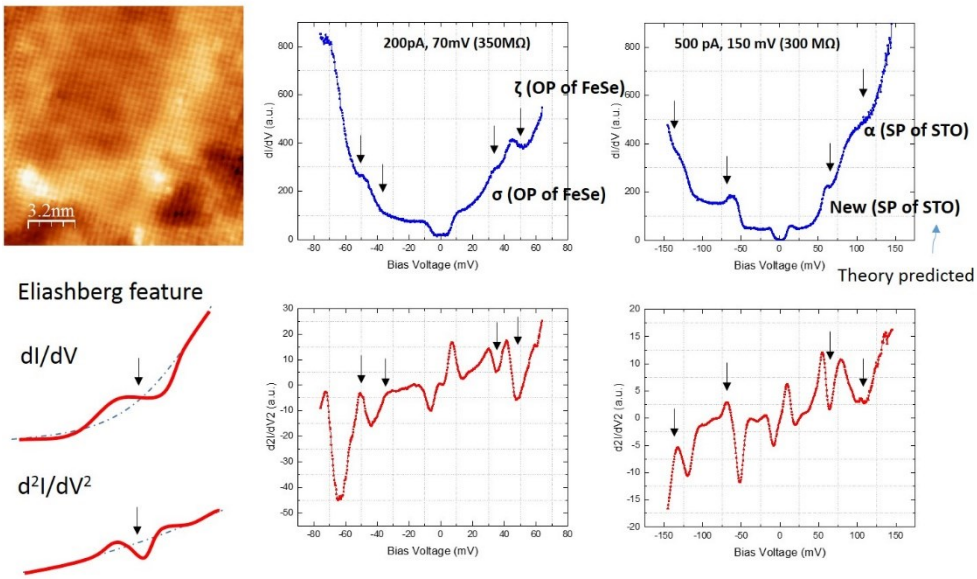

Figure 44 High Energy Spectroscopy with Eliashberg feature

Chapter 5. STM Study of hexagonal FeSe on SrTiO3(100)

5.1 Introduction

5.1.1 Various Phase of FeSe

FeSe appears in various structures besides the tetragonal structure studied in the previous chapter. A typical phase of FeSe through binary phase diagram of Fe and Se is as follows.

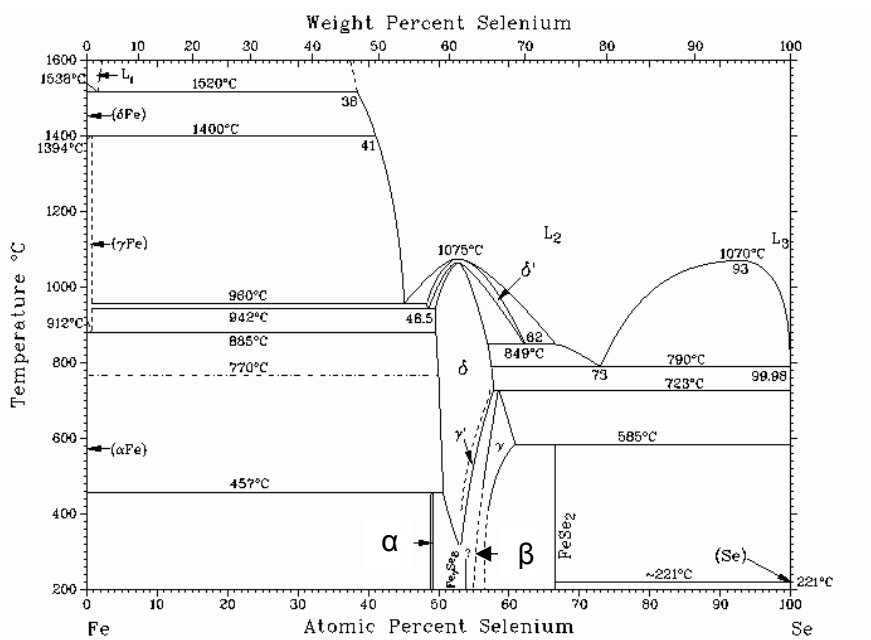

Figure 45 Binary Phase Diagram of FeSe

Image taken from [63]

The phases shown in the binary phase diagram (Figure 45) are summarized as follows.

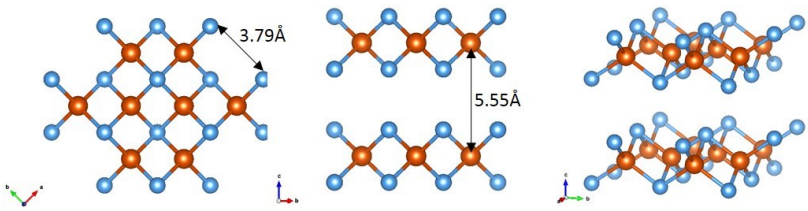

Figure 46 α-FeSe : tetragonal PbO-structure

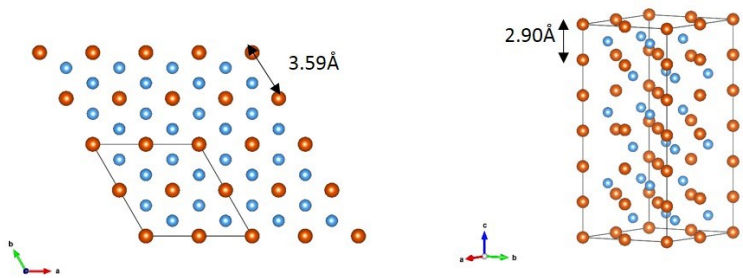

Figure 47 β-FeSe : hexagonal Fe_7Se_8

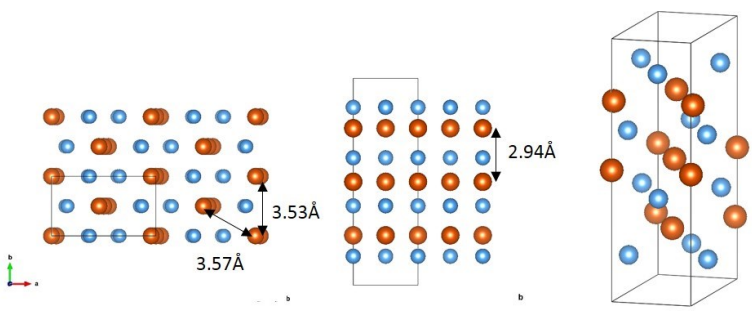

Figure 48 γ-FeSe : monoclinic Fe_3Se_4

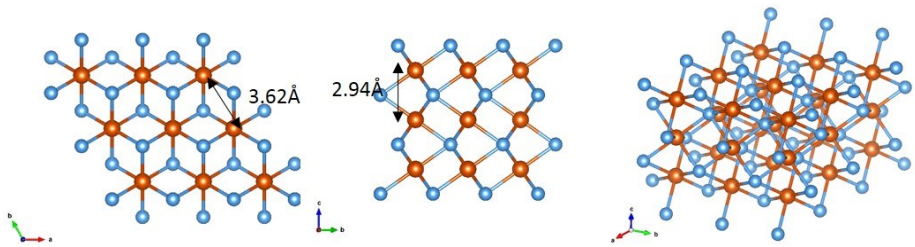

Figure 49 δ-FeSe : hexagonal NiAs-structure

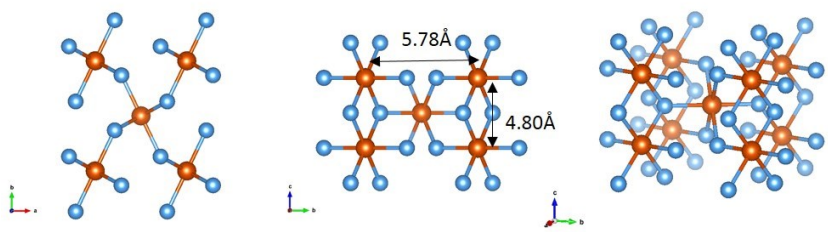

Figure 50 $FeSe_2$: marcasite structure

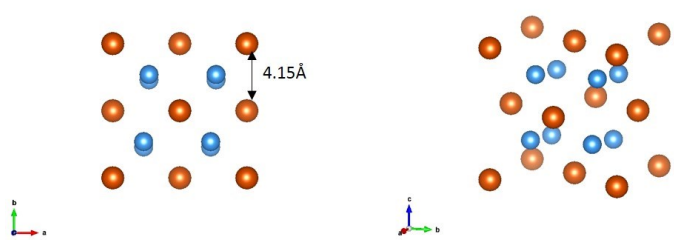

Figure 51 $FeSe_2$: pyrite structure at high pressure & high temperature

5.1.2 Hexagonal Phase of FeSe

In this section, I will look at the hexagonal phase of FeSe in many of the phases introduced in the previous section. Hexagonal FeSe corresponds to

the β and δ phases in the binary phase diagram. The β phase is Fe_7Se_8 and the lattice constant a = b = 3.59 Å, c = 2.9 Å. The δ phase is a NiAs-structure with lattice constant a = b = 3.62 Å, c = 2.94 Å. According to previous studies, hexagonal $FeSe_x$ is known as ferrimagnet [64]. The structure and properties of bulk hexagonal FeSe have been studied by Japanese researchers in the 1950-1960s [65]. As of 2017, 1ML hexagonal FeSe is grown on tetragonal FeSe or $SrTiO_3$ (100) and physical properties estimated as superconductor are emerging. In the next section, I will introduce the STM experimental results.

5.2 Experimental Results

5.2.1 Structure and Spectroscopy of hexagonal FeSe

In this section, we present the results of the STM study on hexagonal FeSe newly grown on $SrTiO_3$(100). It is still unclear how the hexagonal phase grew, and I am working on a follow-up study. However, the Fe and Se ratios are different from those when the tetragonal FeSe is grown but the temperature conditions are not significantly different. The hexagonal FeSe grows in island form on SrTiO3 as shown in Figure 52 and can be confirmed as hexagonal structure through atomic image. It can be seen from the spectroscopy that there is a zero-bias gap and a superconductor-like peaks or shoulders to the left and right of the gap. This is a clue that a hexagonal FeSe thin film cloud be a superconductor.

In some regions, island is formed as shown in Figure 53. The atomic

structure is also hexagonal and the spectroscopy is the same as the one introduced in the previous paragraph. After annealing the sample more, which was not exposed to the substrate, we observed again that the hexagonal phase was grown on the tetragonal phase. STM Image and spectroscopy were performed to investigate whether the bottom tetragonal phase is $SrTiO_3$ or tetragonal FeSe. The result is shown in Figure 54 and it is believed to be tetragonal FeSe, not $SrTiO_3$. Before discussing the reason, I would like to mention that tetragonal FeSe may not be superconducting [54]. Therefore, it cannot be concluded that the superconducting feature does not appear in the spectroscopy and it is not tetragonal FeSe. Several studies have suggested that the substrate is tetragonal FeSe rather than SrTiO3. Unlike the STM study on $SrTiO_3$ previously performed, the atomic structure was reliably resolved and the surface corrugation was less than the $SrTiO_3$ surface. And most of all, the negative islands shown in Figure 54 could not be seen in the $SrTiO_3$. Therefore, it is thought that hexagonal FeSe is grown on non-superconducting tetragonal FeSe. Also, the superconducting gap feature is similar on the terrace where the hexagonal FeSe is grown as a thick island as shown in Figure 55.

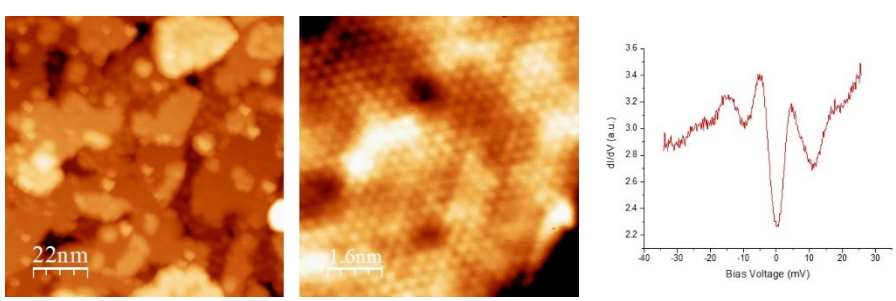

Figure 52 STM Image and Spectroscopy of hexagonal FeSe

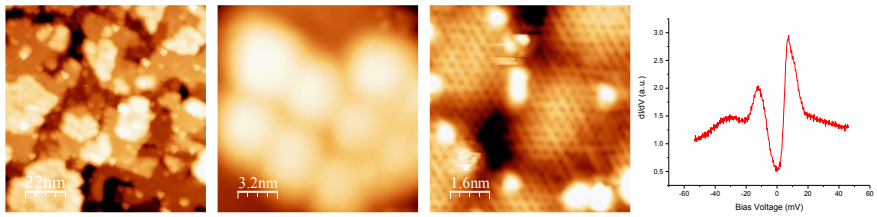

Figure 53 STM Image and Spectroscopy of few ML hexagonal FeSe

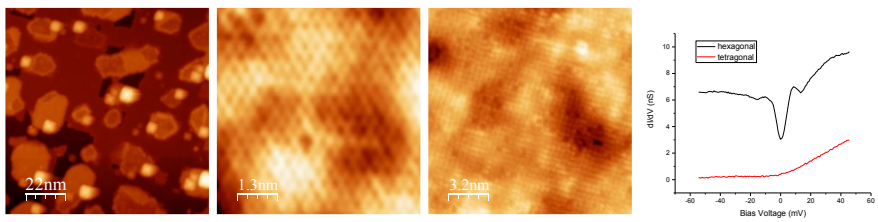

Figure 54 STM Image and Spectroscopy of hexagonal FeSe islands on tetragonal FeSe

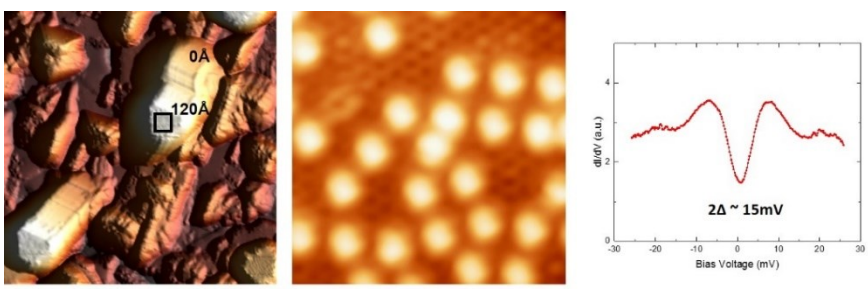

Figure 55 STM Image and Spectroscopy of a thick-layer FeSe island

5.2.2 Possibility as a New Superconductor

In the previous section, it was confirmed through STM spectroscopy that hexagonal FeSe could be a superconductor. In this section, I will introduce

another evidence that hexagonal FeSe could be a superconductor. Figure 56 shows that the gap of spectroscopy is reduced by Fe cluster and unidentified impurity. A similar phenomenon appears in the superconductor, which means that superconductivity is weakened by magnetic impurity. Figure 57 shows that the gap size can be changed by the difference of the Moiré due to the interaction with the sub-surface. Tetragonal FeSe has been suggested to have improved superconductivity due to the interface effect with the $SrTiO_3$ surface. This measurement also shows that the relationship with the interface could affect the superconductivity.

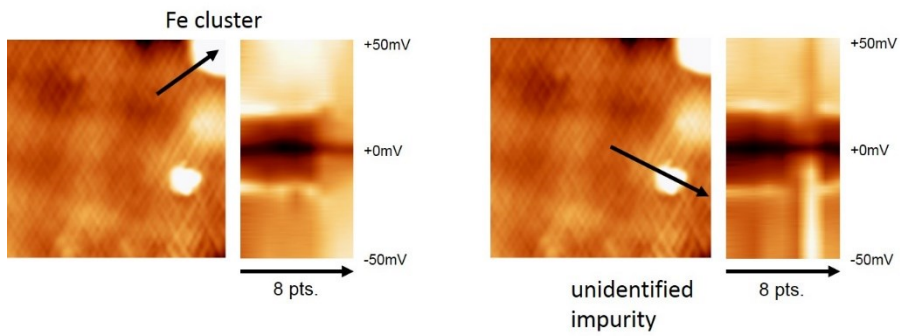

Figure 56 hexagonal FeSe : Possibility as a new Superconductor

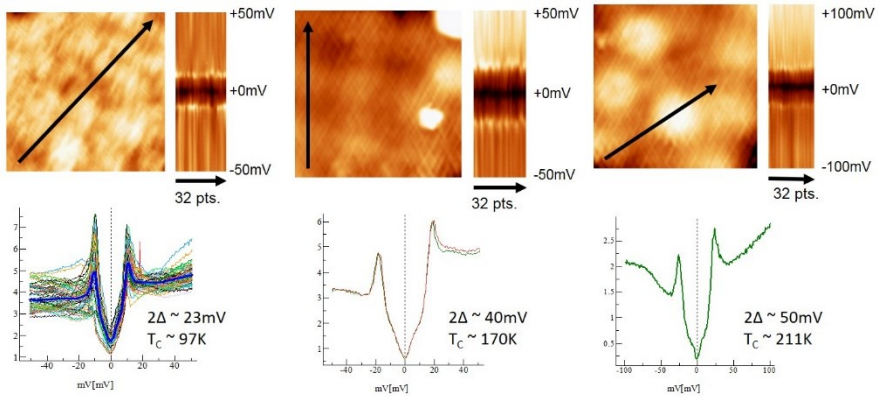

Gap and Sub-surface

T_C is calculated from $2\Delta/k_B T_C$=5.5 (bulk tet-FeSe)

Figure 57 STM Spectroscopy of hexagonal FeSe and Sub-surface

Chapter 6. Conclusion

I have studied FeSe, one of the iron-based high-temperature superconductors, using a scanning tunneling microscope (STM). For the study of superconductivity, ultra-high vacuum and cryogenic STM was built directly from design to assembly, and superconductivity research was carried out on this home-built equipment. The tetragonal FeSe was grown on $SrTiO_3$(100) substrate to reproduce the spectroscopy and electronic structure already studied by the other researchers, and to observe the Eliashberg feature which was not seen in previous research. Previous APRES and EELS [60] studies show that the surface phonon mode of $SrTiO_3$(100) at 92 meV is the main bosonic mode mediating the Cooper pair.

Here, the results of this study suggest that both the acoustic and optical phonon modes of FeSe and various surface phonon modes of $SrTiO_3$ are also mediate Cooper pairing. I also plan to analyze the percentage of each bosonic mode participating in pairing with Eliashberg model fitting. The present study further suggests the discovery of hexagonal FeSe which can be studied after tetragonal FeSe and the possibility of superconductivity of this material.

Appedix. A. Study of (√3×√3)R30°-Se/Au(111)

I made a regular structure with Se atoms on Au(111) single crystal (Figure 58). According to previous study [66], this structure is expected to be (√3×√3)R30°-Se. One observation is that the Se atoms have been sprayed and the herringbone structure of Au(111) has disappeared. I (tunneling current) - Z (tip-sample distance) curve was obtained on the Au surface of this sample and on the Se atomic structure. Scaling the current to log and plotting the tip-sample distance along the x-axis yields as shown in Figure 59. Z Offset Fitting from 0 pm to 300 pm with I = a exp(-kz) yields k = 0.0216 (/ pm) on Au surface. From this value and the tunneling equation $k = 2\sqrt{(2m\phi)}/\hbar$, we can see that the work function Φ = 4.40 eV. In the same way, the work function Φ on Se is obtained from the I-Z curve, which is Φ = 4.52 eV. Work function on Au is 0.12 eV larger than that on Se.

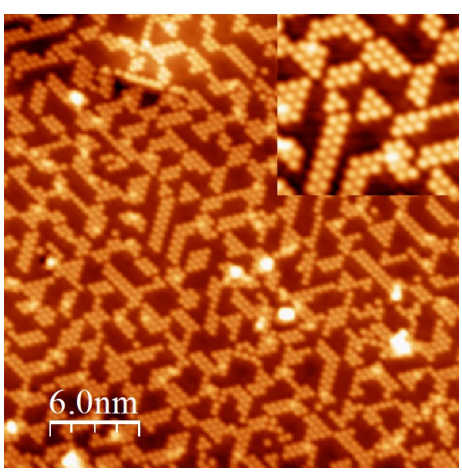

Figure 58 Topographic Image of (√3×√3)R30°-Se on Au(111)

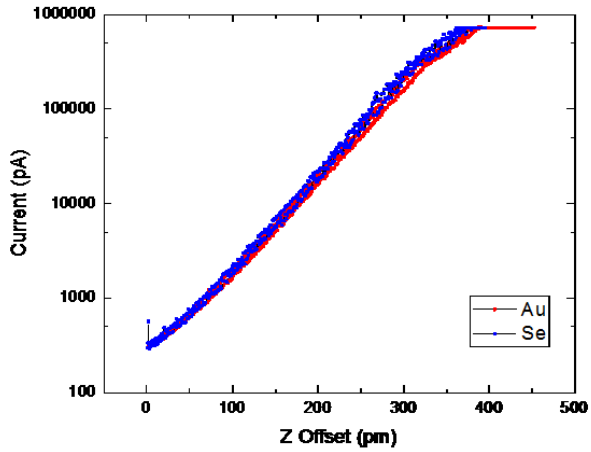

Figure 59 I-Z curve on Se/Au(111)

Figure 60 shows two spectroscopies on Se atoms and Au surface, respectively. On Au surface, the surface state disappears and a new state appears near the zero bias. On the Se atoms, the state appears near -600 mV. Let's look at the case of a simple atomic rhombus structure like the topographic image in Figure 61. Spectroscopy at the center of the Rhombus structure is shown in the top-right plot. There are a few states, and I get the dI/dV maps for each energy, which are the dI/dV Maps in Figure 61. It can be seen that the distribution of electrons changes with each bias voltage, and it is expected to be a kind of quantum confinement states.

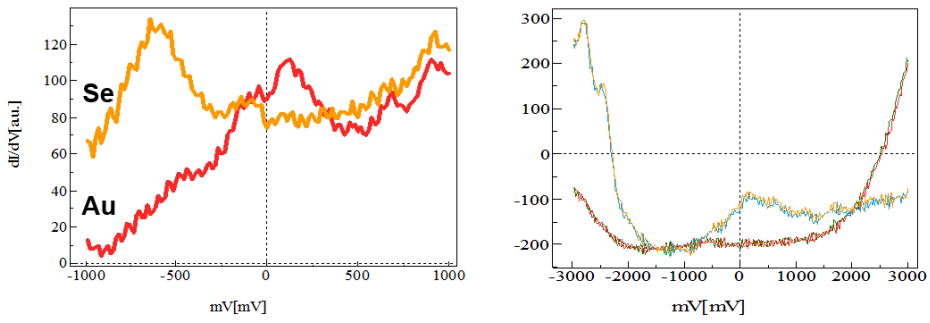

Figure 60 STM Spectroscopy on Se/Au(111)

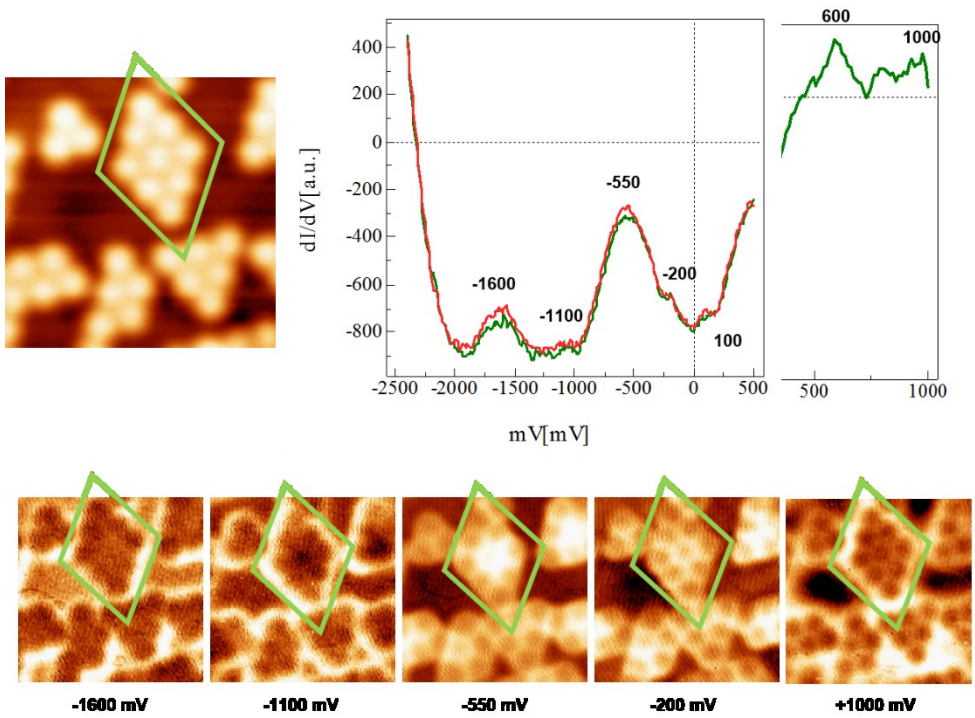

Figure 61 Quantum Confinement on Se Rhombus Structure

Appedix. B. Various Phase of CuSe on Cu(111)

After depositing Se on Cu (111), annealing to 300 ~ 400 ℃ resulted in various CuSe phases as shown in Figure 62. Compared with the binary alloy phase diagram of Cu-Se, each structure is estimated to be hexagonal α phase CuSe, pyrite $CuSe_2$, and Se atomic structure on Cu (111).

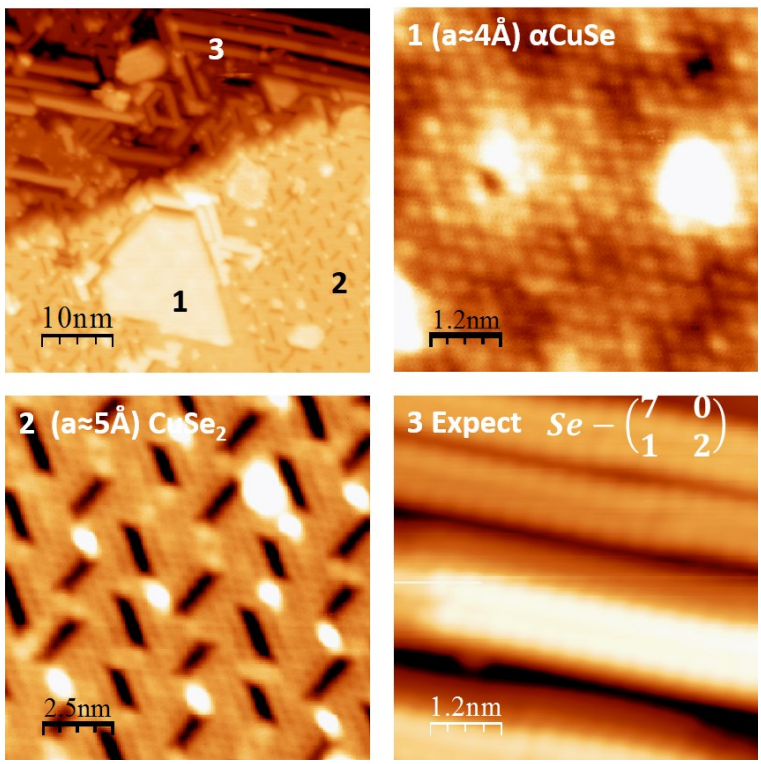

Figure 62 Various Phases of Copper Selenide

Appedix. C. Magnetic Domain on Co/Pt(111)

Cobalt is deposited on Pt(111) single crystal and annealed to form islands as shown in Figure 63. On top of the island, Moiré pattern and hexagonal atomic structure are obtained by STM. Using Cr-tip, some islands have two different conductance areas as shown in Figure 64. At different sample bias voltage, I can get different conductance map. By analyzing the area where conductance is inverted, the width of the magnetic domain wall could be measured. And it is about 1 nm. This is very thin magnetic domain wall width.

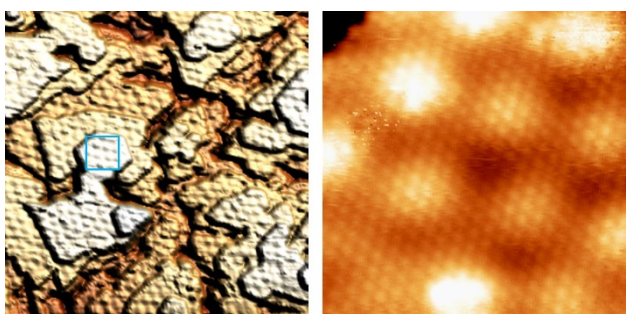

Figure 63 Cobalt Islands on Pt(111) and its atomic structure

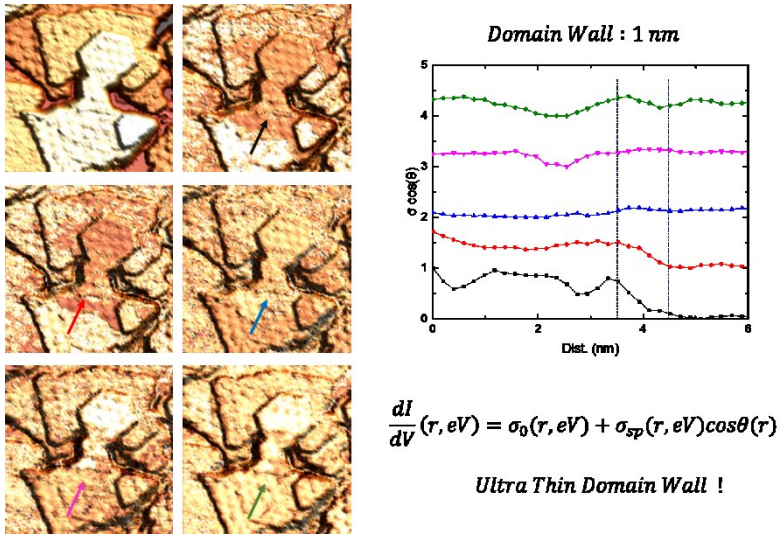

Figure 64 Magnetic Domain Wall of Co island on Pt(111)

Bibliography

[1] H. K. Onnes, "Superconductivity," *Commun Phys Lab Univ Leiden*, vol. 120b, 122b, 124c, 1911.

[2] W. Qing-Yan *et al.*, "Interface-Induced High-Temperature Superconductivity in Single Unit-Cell FeSe Films on SrTiO3," *Chin. Phys. Lett.*, vol. 29, no. 3, p. 037402, Mar. 2012.

[3] J. G. Bednorz and K. A. Müller, "Possible highTc superconductivity in the Ba−La−Cu−O system," *Z. Für Phys. B Condens. Matter*, vol. 64, no. 2, pp. 189–193, Jun. 1986.

[4] Y. Kamihara, T. Watanabe, M. Hirano, and H. Hosono, "Iron-Based Layered Superconductor La[O1-xFx]FeAs (x = 0.05−0.12) with Tc = 26 K," *J. Am. Chem. Soc.*, vol. 130, no. 11, pp. 3296–3297, Mar. 2008.

[5] J. Bardeen, L. N. Cooper, and J. R. Schrieffer, "Theory of Superconductivity," *Phys. Rev.*, vol. 108, no. 5, pp. 1175–1204, Dec. 1957.

[6] "Superconductivity," *Wikipedia*. 07-Jun-2017.

[7] M. P. Schackert, *Scanning Tunneling Spectroscopy on Electron-Boson Interactions in Superconductors*. Karlsruhe, Baden: KIT Scientific Publishing, 2015.

[8] "SQUID," *Wikipedia*. 09-Jun-2017.

[9] N. W. Ashcroft and N. D. Mermin, *Solid state physics*. New York: Holt, Rinehart and Winston, 1976.

[10] W. Meissner and R. Ochsenfeld, "Ein neuer Effekt bei Eintritt der Supraleitfähigkeit," *Naturwissenschaften*, vol. 21, no. 44, pp. 787–788, Nov. 1933.

[11] F. London and H. London, "The Electromagnetic Equations of the Supraconductor," *Proc. R. Soc. Lond. Math. Phys. Eng. Sci.*, vol. 149, no. 866, pp. 71–88, Mar. 1935.

[12] V. L. Ginzburg and L. D. Landau, "On the theory of superconductivity," *Zh Eksp Teor Fiz*, vol. 20, pp. 1064–1082.

[13] A. A. Abrikosov, "On the Magnetic Properties of Superconductors of the Second Group," *Sov Phys JETP*, vol. 5, p. 1174, 1957.

[14] E. Maxwell, "Isotope Effect in the Superconductivity of Mercury," *Phys. Rev.*, vol. 78, no. 4, pp. 477–477, May 1950.

[15] M. Tinkham, *Introduction to Superconductivity: Second Edition*, 2 edition. Mineola, NY: Dover Publications, 2004.

[16] D. J. Scalapino, J. R. Schrieffer, and J. W. Wilkins, "Strong-Coupling Superconductivity. I," *Phys. Rev.*, vol. 148, no. 1, pp. 263–279, Aug. 1966.

[17] S. Grothe, S. Johnston, S. Chi, P. Dosanjh, S. A. Burke, and Y. Pennec, "Quantifying Many-Body Effects by High-Resolution Fourier Transform Scanning Tunneling Spectroscopy," *Phys. Rev. Lett.*, vol. 111, no. 24, p.

246804, Dec. 2013.
[18] G. M. Eliashberg, “Interactions between Electrons and Lattice Vibrations in a Superconductor,” *JETP*, vol. 11, p. 696.
[19] “Milestone Superconductivity Above 200 Celsius.” [Online]. Available: http://www.superconductors.org/202C.htm. [Accessed: 12-Jun-2017].
[20] F. Steglich *et al.*, “Superconductivity in the Presence of Strong Pauli Paramagnetism: CeCu2Si2,” *Phys. Rev. Lett.*, vol. 43, no. 25, pp. 1892–1896, Dec. 1979.
[21] L. Shan *et al.*, “Evidence of a Spin Resonance Mode in the Iron-Based Superconductor Ba0.6K0.4Fe2As2 from Scanning Tunneling Spectroscopy,” *Phys. Rev. Lett.*, vol. 108, no. 22, p. 227002, May 2012.
[22] Y. Saito, T. Nojima, and Y. Iwasa, “Highly crystalline 2D superconductors,” *Nat. Rev. Mater.*, vol. 2, no. 1, p. natrevmats201694, Dec. 2016.
[23] G. Benedek *et al.*, “Theory of surface phonons at metal surfaces: recent advances,” *J. Phys. Condens. Matter*, vol. 22, no. 8, p. 084020, 2010.
[24] S. H. Pan, WO 93/19494, 30-Sep-1993.
[25] K. Besocke, “An easily operable scanning tunneling microscope,” *Surf. Sci.*, vol. 181, no. 1, pp. 145–153, Mar. 1987.
[26] I. Giaever, “Electron Tunneling and Superconductivity,” *Science*, vol. 183, no. 4131, pp. 1253–1258, Mar. 1974.
[27] J. E. Hoffman, “Spectroscopic scanning tunneling microscopy insights into Fe-based superconductors,” *Rep. Prog. Phys.*, vol. 74, no. 12, p. 124513, Dec. 2011.
[28] E. L. Wolf, *Principles of Electron Tunneling Spectroscopy*. New York : Oxford Oxforshire: Oxford University Press, 1985.
[29] G. Binnig, H. Rohrer, C. Gerber, and E. Weibel, “Surface Studies by Scanning Tunneling Microscopy,” *Phys. Rev. Lett.*, vol. 49, no. 1, pp. 57–61, Jul. 1982.
[30] R. C. Jaklevic and J. Lambe, “Molecular Vibration Spectra by Electron Tunneling,” *Phys. Rev. Lett.*, vol. 17, no. 22, pp. 1139–1140, Nov. 1966.
[31] “Surface phonon,” *Wikipedia*. 22-Sep-2015.
[32] G. Benedek, W. Kress, and F. W. de Wette, *Surface phonons*. Berlin ; New York : Springer-Verlag, 1991.
[33] H. Gawronski, M. Mehlhorn, and K. Morgenstern, “Imaging Phonon Excitation with Atomic Resolution,” *Science*, vol. 319, no. 5865, pp. 930–933, Feb. 2008.
[34] L. Vitali, M. A. Schneider, K. Kern, L. Wirtz, and A. Rubio, “Phonon and plasmon excitation in inelastic electron tunneling spectroscopy of graphite,” *Phys. Rev. B*, vol. 69, no. 12, p. 121414, Mar. 2004.
[35] B. C. Stipe, M. A. Rezaei, and W. Ho, “Single-Molecule Vibrational Spectroscopy and Microscopy,” *Science*, vol. 280, no. 5370, pp. 1732–1735, Jun. 1998.
[36] A. J. Heinrich, J. A. Gupta, C. P. Lutz, and D. M. Eigler, “Single-Atom Spin-Flip Spectroscopy,” *Science*, vol. 306, no. 5695, pp. 466–469, Oct. 2004.

[37] K. Lahtonen, M. Hirsimäki, M. Lampimäki, and M. Valden, "Oxygen adsorption-induced nanostructures and island formation on Cu{100}: Bridging the gap between the formation of surface confined oxygen chemisorption layer and oxide formation," *J. Chem. Phys.*, vol. 129, no. 12, p. 124703, Sep. 2008.
[38] T. Fujita, Y. Okawa, Y. Matsumoto, and K. Tanaka, "Phase boundaries of nanometer scale c(2x2)-O domains on the Cu(100) surface," *Phys. Rev. B*, vol. 54, no. 3, pp. 2167–2174, Jul. 1996.
[39] C. Wöll, R. J. Wilson, S. Chiang, H. C. Zeng, and K. A. R. Mitchell, "Oxygen on Cu(100) surface structure studied by scanning tunneling microscopy and by low-energy-electron-diffraction multiple-scattering calculations," *Phys. Rev. B*, vol. 42, no. 18, pp. 11926–11929, Dec. 1990.
[40] M. Wuttig, R. Franchy, and H. Ibach, "Oxygen on Cu(100) – a case of an adsorbate induced reconstruction," *Surf. Sci.*, vol. 213, no. 1, pp. 103–136, Apr. 1989.
[41] F. M. Leibsle, "STM studies of oxygen-induced structures and nitrogen coadsorption on the Cu(100) surface: evidence for a one-dimensional oxygen reconstruction and reconstructive interactions," *Surf. Sci.*, vol. 337, no. 1, pp. 51–66, Aug. 1995.
[42] M. Z. Baykara *et al.*, "Atom-specific forces and defect identification on surface-oxidized Cu(100) with combined 3D-AFM and STM measurements," *Phys. Rev. B*, vol. 87, no. 15, p. 155414, Apr. 2013.
[43] J. S. Nelson, E. C. Sowa, and M. S. Daw, "Calculation of Phonons on the Cu(100) Surface by the Embedded-Atom Method," *Phys. Rev. Lett.*, vol. 61, no. 17, pp. 1977–1980, Oct. 1988.
[44] M. Alcántara Ortigoza, R. Heid, K.-P. Bohnen, and T. S. Rahman, "Effect of c(2x2)-CO overlayer on the phonons of Cu(001): A first-principles study," *Phys. Rev. B*, vol. 79, no. 12, p. 125432, Mar. 2009.
[45] L. Vitali, S. D. Borisova, G. G. Rusina, E. V. Chulkov, and K. Kern, "Inelastic electron tunneling spectroscopy: A route to the identification of the tip-apex structure," *Phys. Rev. B*, vol. 81, no. 15, p. 153409, Apr. 2010.
[46] M. J. Harrison, D. P. Woodruff, J. Robinson, D. Sander, W. Pan, and J. Kirschner, "Adsorbate-induced surface reconstruction and surface-stress changes in Cu(100)/O: Experiment and theory," *Phys. Rev. B*, vol. 74, no. 16, p. 165402, Oct. 2006.
[47] B. N. J. Persson and A. Baratoff, "Inelastic electron tunneling from a metal tip: The contribution from resonant processes," *Phys. Rev. Lett.*, vol. 59, no. 3, pp. 339–342, Jul. 1987.
[48] F.-C. Hsu *et al.*, "Superconductivity in the PbO-type structure α-FeSe," *Proc. Natl. Acad. Sci.*, vol. 105, no. 38, pp. 14262–14264, Sep. 2008.
[49] S. Tan *et al.*, "Interface-induced superconductivity and strain-dependent spin density waves in FeSe/SrTiO3 thin films," *Nat. Mater.*, vol. 12, no. 7, pp. 634–640, Jul. 2013.

[50] T. Hanaguri, S. Niitaka, K. Kuroki, and H. Takagi, “Unconventional s-Wave Superconductivity in Fe(Se,Te),” *Science*, vol. 328, no. 5977, pp. 474–476, Apr. 2010.
[51] C.-L. Song *et al.*, “Molecular-beam epitaxy and robust superconductivity of stoichiometric FeSe crystalline films on bilayer graphene,” *Phys. Rev. B*, vol. 84, no. 2, p. 020503, Jul. 2011.
[52] J.-F. Ge *et al.*, “Superconductivity above 100 K in single-layer FeSe films on doped SrTiO3,” *Nat. Mater.*, vol. 14, no. 3, pp. 285–289, Mar. 2015.
[53] D. Huang and J. E. Hoffman, “Monolayer FeSe on SrTiO3,” *Annu. Rev. Condens. Matter Phys.*, vol. 8, no. 1, pp. 311–336, 2017.
[54] Z. Li *et al.*, “Molecular beam epitaxy growth and post-growth annealing of FeSe films on SrTiO 3 : a scanning tunneling microscopy study,” *J. Phys. Condens. Matter*, vol. 26, no. 26, p. 265002, 2014.
[55] Q. Fan *et al.*, “Plain s-wave superconductivity in single-layer FeSe on SrTiO3 probed by scanning tunnelling microscopy,” *Nat. Phys.*, vol. 11, no. 11, pp. 946–952, Nov. 2015.
[56] D. Huang *et al.*, “Bounds on nanoscale nematicity in single-layer FeSe/SrTiO3,” *Phys. Rev. B*, vol. 93, no. 12, p. 125129, Mar. 2016.
[57] S. He *et al.*, “Phase diagram and electronic indication of high-temperature superconductivity at 65 K in single-layer FeSe films,” *Nat. Mater.*, vol. 12, no. 7, pp. 605–610, Jul. 2013.
[58] J. He *et al.*, “Electronic evidence of an insulator–superconductor crossover in single-layer FeSe/SrTiO3 films,” *Proc. Natl. Acad. Sci.*, vol. 111, no. 52, pp. 18501–18506, Dec. 2014.
[59] T.-K. Chen *et al.*, “Fe-vacancy order and superconductivity in tetragonal β-Fe1-xSe,” *Proc. Natl. Acad. Sci.*, vol. 111, no. 1, pp. 63–68, Jan. 2014.
[60] S. Zhang *et al.*, “Role of SrTiO3 phonon penetrating into thin FeSe films in the enhancement of superconductivity,” *Phys. Rev. B*, vol. 94, no. 8, p. 081116, Aug. 2016.
[61] Y. Xie, H.-Y. Cao, Y. Zhou, S. Chen, H. Xiang, and X.-G. Gong, “Oxygen Vacancy Induced Flat Phonon Mode at FeSe /SrTiO3 interface,” *Sci. Rep.*, vol. 5, Jun. 2015.
[62] “Electronic structure and superconductivity of FeSe-related superconductors - IOPscience.” [Online]. Available: http://iopscience.iop.org/article/10.1088/0953-8984/27/18/183201. [Accessed: 19-Jul-2017].
[63] B. Predel, “Fe-Se (Iron-Selenium),” in *Dy-Er – Fr-Mo*, O. Madelung, Ed. Springer Berlin Heidelberg, 1995, pp. 1–4.
[64] “On the Ferrimagnetism of Iron Selenides,” *J. Phys. Soc. Jpn.*, vol. 9, no. 4, pp. 496–499, Jul. 1954.
[65] “The Superstructures of Iron Selenide Fe7Se8,” *J. Phys. Soc. Jpn.*, vol. 16, no. 6, pp. 1162–1170, Jun. 1961.

[66] K. Schouteden, J. Debehets, D. Muzychenko, Z. Li, J. W. Seo, and C. V. Haesendonck, “Adsorption of Te atoms on Au(1 1 1) and the emergence of an adatom-induced bound state,” *J. Phys. Condens. Matter*, vol. 29, no. 12, p. 125001, 2017.

국 문 초 록

박막 아이언 셀레나이드 초전도체
: 주사형 탐침 현미경 연구

이민준

물리천문학부

서울대학교 대학원

1911년, H. K. Onnes 에 의해서 초전도 현상이 발견된 이후 [1], 초전도체는 고체물리학의 주요한 연구 분야로 자리매김하였다. 수많은 물리학자들이 새로운 초전도체를 발견해왔고, 물리학적으로 초전도 현상을 설명하기 위해서 일하고 있다. 표면과학에서도 초전도체는 흥미로운 연구 주제이다. 표면과학에서는 어떻게 저차원 물리현상이 초전도체에서 나타나는가와 어떻게 초전도 현상이 저차원에서 변화하는가를 주로 연구한다. 나는 주사현 검침 현미경 (STM) 을 사용하여 특별히 이차원에서 나타나는 초전도 현상을 연구하였다. 본 연구에 사용된 초전도 샘플은 $SrTiO_3$(100) 기판 위에 키워진 정사각형의 FeSe 와 같은 기판 위에 키워진 육각형의 FeSe 이다. 정사각형 FeSe 는 철 칼코겐 초전도체 중에서 가장 단순한 구조를 가지고 있다. 2012년, 중국의 Xue 그룹에서 정사각형

FeSe 한 층을 $SrTiO_3$(100) 기판 위에 키웠을 때 초전도 임계 온도가 60 K 이상으로 올라가는 것을 발견하였고 [2], 많은 물리학자들이 이 연구에 뛰어들어서 왜 임계 온도가 향상되었는지를 연구해왔다. 본 연구는 $SrTiO_3$(100) 기판 위의 정사각형 FeSe 에서의 페어링 메커니즘을 밝히기 위해서 시작되었다. 나는 주사형 탐침 현미경의 스펙트로스코피를 분석했고 Eliashberg 모델을 사용하여 쿠퍼 페어링에 관계된 보조닉 보드의 주파수를 찾았다. 그리고 나는 보조닉 모드의 정체가 무엇인지 알아내기 위해서 노력했다. 다음으로 $SrTiO_3$(100) 기판 위에 FeSe 의 새로운 상인 육각형 구조의 FeSe 를 키웠고 이 물질의 물리적 특성을 주사형 탐침 현미경을 사용하여 측정하였다. 새롭게 발견된 육각형 구조의 FeSe 는 초전도 현상과 일치하는 많은 실험 결과를 보여준다. 그러나 이 물질이 새로운 초전도체인지를 확인하기 위해서는 더 많은 연구가 필요하다.

주요어 : 초전도체, 박막 초전도체, 철 셀레나이드, 주사형 탐침 현미경

학 번 : 2009-20420